DLR Design Challenge 2022

INFERNO

INtelligent **F**ir**E** **R**espo**N**se **O**peration

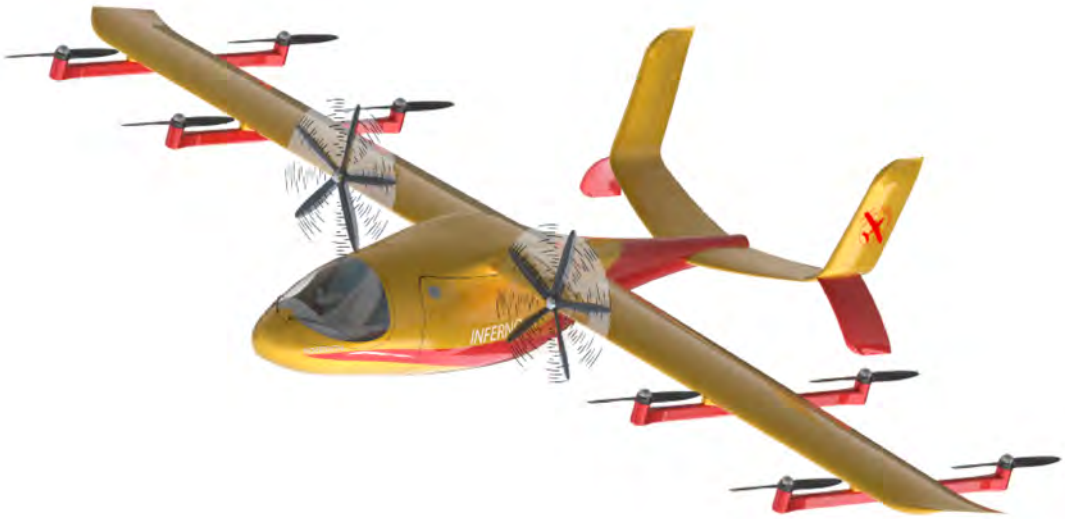

Aerial Firefighting Aircraft

Team Stuttgart
Ahmet Günay Can
Hannes Kahlo
Benjamin Knoblauch
Nicolas Mandry
Prishit Modi
Johannes Ritter

Academic Support and Advisors
Prof. Dr. Andreas Strohmayer
M.Sc. Johannes Schneider

Submitted on July 11th, 2022

Team Members

Ahmet Günay Can, B.Sc.
Aerospace Engineering
1st semester

Hannes Kahlo, B.Sc.
Aerospace Engineering
4th semester

Benjamin Knoblauch, B.Sc.
Aerospace Engineering
2nd semester

Nicolas Mandry, B.Sc.
Aerospace Engineering
4th semester

Prishit Modi, B.Eng.
Aerospace Engineering
3rd semester

Johannes Ritter, B.Sc.
Aerospace Engineering
4th semester

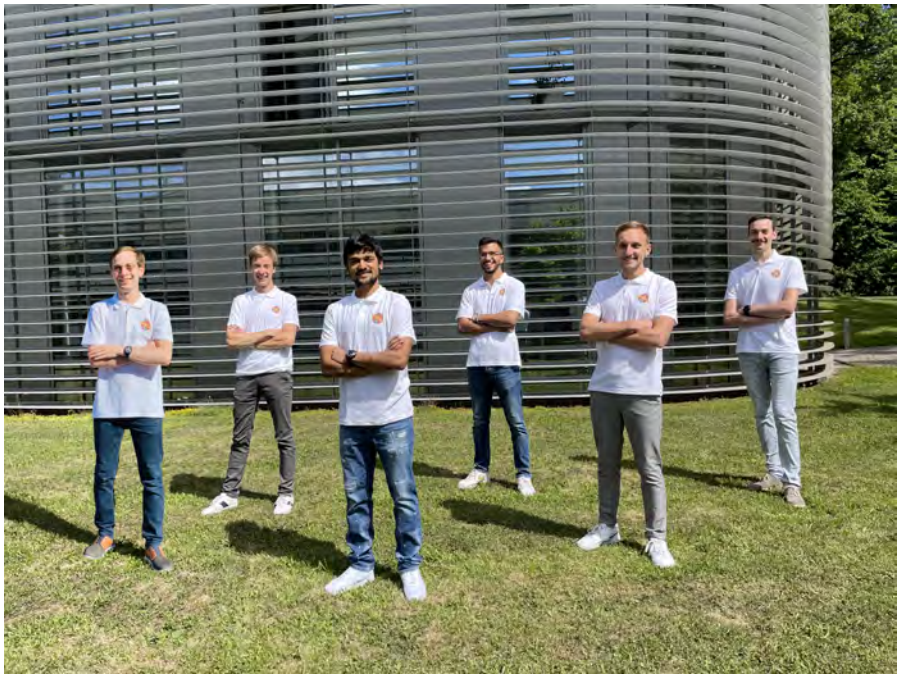

Universität Stuttgart

Institut für Flugzeugbau

Institutsleitung
Prof. Dr. Peter Middendorf
Prof. Dr. Po Wen Cheng
Prof. Dr. Andreas Strohmayer

Universität Stuttgart
Institut für Flugzeugbau • Pfaffenwaldring 31 • 70569 Stuttgart

Kontakt
Johannes Schneider
Pfaffenwaldring 31
70569 Stuttgart
T 0711 685-60483
F 0711 685-62449
E-Mail:
schneider@ifb.uni-stuttgart.de
www.ifb.uni-stuttgart.de

Betreff: Bestätigungsschreiben

11.07.2022

Sehr geehrte Damen und Herren,

hiermit bestätige ich, dass die im Folgenden aufgeführten Mitglieder des studentischen Teams selbstständig den Flugzeugentwurf zur Teilnahme an der NASA/DLR-Design Challenge 2022 durchgeführt haben.

- Benjamin Knoblauch
- Günay Can
- Hannes Kahlo
- Johannes Ritter
- Modi Prishit
- Nicolas Mandry

Mit freundlichen Grüßen,

Johannes Schneider

Betreuender wissenschaftlicher Mitarbeiter

Abstract

The aviation industry has always been shaped by the constant strive for improvements and state-of-the-art innovations in order to combine an economical and ecological motivation with a relentless effort to ensure safety in our skies and contribute to the well-being of our society. By using revolutionary technologies, new aircraft projects can thus contribute to fight climate change and even assist in special and demanding operations like firefighting. **IN**telligent **F**ir**E** **R**espo**N**se **O**peration (INFERNO) is a fleet of four **V**ertical **T**ake-**O**ff and **L**anding (VTOL) aircraft operating together interconnected and intelligently for efficient, next generation aerial firefighting with an expected **E**ntry **I**nto-**S**ervice (EIS) in 2030.
The project and this report is part of the 2022 DLR Design Challenge covering the preliminary design including the structural concept, aerodynamic simulations, sizing and selection of the hybrid powertrain, weight and balance calculations and the concept for water intake and deployment. Furthermore, profound considerations were taken into account regarding additional wildfire scenarios, the operational concept and yearly aerial firefighting demand in Europe and the US. For the development, extensive literature research, as well as textbook methods and detailed aerodynamic simulations were utilized.
The designed aircraft is characterized by a considerable high payload ratio that features vertical take-off and landing capabilities while showing efficient horizontal flight properties with a very competitive cost basis. The 24 h operability during various weather conditions and during challenging fire scenarios is ensured using a wide variety of sensors and a modern glass-cockpit combining pilot comfort with indispensable safety aspects. Due to its modular design, every aircraft can be comfortably converted to a passenger or freight version during firefighting off-season or for cargo and crew supply during the missions.

Kurzzusammenfassung

Die Luftfahrtindustrie ist seit jeher durch das ständige Streben nach Verbesserungen und neuesten Innovationen geprägt, um eine ökonomische und ökologische Verbesserung mit der kontinuierlichen Steigerung der Sicherheit im Luftraum zu verbinden. INFERNO ist eine Flotte von vier VTOL-Flugzeugen, die vernetzt und intelligent für eine effiziente Brandbekämpfung aus der Luft der nächsten Generation zusammenarbeiten und im Jahr 2030 einsatzbereit sein werden.
Das Projekt ist Teil der DLR Design Challenge 2022, und dieser Bericht umfasst den vorläufigen Entwurf, insbesondere das Strukturkonzept, aerodynamische Simulationen, Dimensionierung und Auswahl des Hybridantriebsstrangs, Gewichts- und Schwerpunktberechnungen sowie das Konzept für Wasseraufnahme- und ausbringung. Darüber hinaus werden weitere detaillierte Recherchen zu zusätzlichen Waldbrandszenarien, dem Einsatzkonzept und dem jährlichen Bedarf an Brandbekämpfung aus der Luft in Europa und den USA vorgestellt. Für die Entwicklung wurden umfangreiche Literaturrecherchen, Lehrbuchmethoden und aerodynamische Simulationen herangezogen.
Das Resultat ist ein Flugzeug mit einem sehr hohen Nutzlastverhältnis, das sowohl vertikale Starts und Landungen als auch einen effizienten Horizontalflug mit einer sehr wettbewerbsfähigen Kostenbasis vereint. Der 24-Stunden-Einsatz wird durch eine Vielzahl von Sensoren und einem modernen Glascockpit gewährleistet, das Pilotenkomfort und Sicherheit garantiert. Aufgrund der modularen Bauweise kann das Flugzeug in der Waldbrand Nebensaison in eine Passagier- oder Frachtversion umgerüstet werden.

Contents

List of Figures VI

List of Tables VIII

List of Abbreviations IX

Greek Symbols and Variables XI

1 Introduction 1

2 Wildfire Scenarios 1
2.1 Initial Sizing – Maximizing Dumped Water . . . 2

3 Design Process 3
3.1 Vertical Take-Off and Landing vs. Short Take-Off and Landing . . . 3
3.2 Fuel Type and Energy Storage Concept . . . 3
3.3 Configuration Selection and Key Technologies . . . 4

4 INFERNO Configuration & Features 5
4.1 Aerodynamics and Flight Mechanics . . . 5
4.1.1 Wing Planform Selection . . . 5
4.1.2 Morphing Wing . . . 6
4.1.3 Airfoil Selection . . . 6
4.1.4 Aerodynamic Calculations of the Aircraft . . . 7
4.1.5 Tail . . . 8
4.2 Propulsion and Battery . . . 9
4.2.1 Calculation of Power Demand . . . 9
4.2.2 The Hybrid Configuration . . . 10
4.2.3 Powerplant Selection . . . 11
4.2.4 Propeller and Electric Motor Selection . . . 11
4.2.5 Battery Sizing . . . 12
4.2.6 Fuel Tank Sizing . . . 12
4.2.7 Engine Air Intake and Exhaust . . . 13
4.3 Mass Calculation and Balance . . . 13
4.4 Cockpit . . . 15
4.5 Sensing Instruments . . . 16
4.6 Water Pick-Up and Dropping . . . 16
4.7 Structure and Loads . . . 18
4.7.1 Structural Concept of the Aircraft . . . 18
4.7.2 Structural concept of the modules . . . 18
4.7.3 v-n Diagram . . . 19
4.8 Concept of Water Tank . . . 19
4.9 Noise Reduction . . . 19
4.10 Minimising Hazards and Failures . . . 20
4.11 Configuration Summary . . . 20

5 Fleet Concept 20
5.1 Modularity . . . 21
5.2 Operational Concept . . . 21
5.2.1 Operational Concept 24-Hour Mission . . . 22
5.2.2 Annual Operational Concept . . . 22
5.2.3 Formation Flight . . . 23
5.2.4 Aerial Refueling . . . 23
5.2.5 Turnaround and Ground Handling . . . 24

6 Cost Analysis 24
6.1 Life Cycle Cost . . . 24
6.2 Direct Operation Cost . . . 25

7 Evaluation **25**
7.1 Fulfillment of the Design Specifications . . . 25
7.2 Conclusion . . . 25

Bibliography **26**

A Appendix **A1**
A.1 Maps of the Fire Scenarios . . . A1
A.2 Neutral Point Calculation . . . A2
A.3 Visualization of the Module Montage . . . A3
A.4 Battery Sizing: Support Data . . . A4
A.5 INFERNO Cockpit: FOV and Dimensions . . . A5
A.6 Data for Fleet Concept . . . A6
A.7 Tables Representing LCC & DOC . . . A12
A.8 Formulas for Power Demand Calculation . . . A13
A.8.1 Horizontal Take-off Run: . . . A13
A.8.2 Horizontal Climb: . . . A13
A.8.3 Cruise: . . . A13
A.8.4 Horizontal Descend : . . . A13
A.8.5 Hovering: . . . A14
A.8.6 Vertical Ascend and Descend: . . . A14
A.9 Formulas for Weight Calculation . . . A15
A.10 Static Margin and Position of the Center of Gravity . . . A16
A.11 Landing Gear . . . A18
A.12 v-n Diagram . . . A20
A.13 Airfoil Data . . . A21
A.14 INFERNO Immersion . . . A25

List of Figures

2.1 Coast scenario: distance sea – fire source 2

2.2 Coast scenario: distance lake – fire source 2

2.3 Domestic scenario: distance river – fire source 2

2.4 Domestic scenario: distance lake – fire source 2

2.5 Preliminary calculation of the optimal range for water maximization 2

3.1 Unique characteristics of INFERNO 1 4

3.2 Unique characteristics of INFERNO 2 4

3.3 Front view of INFERNO 5

3.4 Top view of INFERNO 5

3.5 Side view of INFERNO 5

4.1 Morphing wing system 6

4.2 Drag polar comparison of E423M and E545 airfoil for $Re = 7.5 \cdot 10^6$ 7

4.3 Calculated Lift to Drag ratio for Cruise and High-Lift Wing Configuration 8

4.4 Distribution of the lift coefficient for cruise flight with different angles of attack 8

4.5 Tailplane arrangement with no angles smaller than 90° for lower interference drag 9

4.6 Power demand for the horizontal and vertical propellers during horizontal and vertical flight 10

4.7 Power demand during transition between vertical and horizontal flight 10

4.8 Illustration of the hybrid energy storage system 11

4.9 Propulsive efficiency comparison for various gas turbine engine configurations 11

4.10 High power Licerion® cell energy across different C-Rates 13

4.11 Static Margin during water and fuel loading with respect to the MAC in the Design Mission 14

4.12 Shift of the CoG during water and fuel loading with respect to the MAC in the Design Mission 14

4.13 INFERNO cockpit design concept with integrated instruments 15

4.14 Structural concept of fuselage with module installed 18

4.15 Structural concept of wing 18

4.16 Structural Concept of Wing and Battery integration 18

4.17 Structural concept of the modules 19

4.18 v-n diagram 19

4.19 Concept of water tank 19

4.20 Payload-Range diagram 20

4.21 Sizing diagram 20

5.1 Cargo version 21

5.2 Passenger version 21

5.3 Fleet concept of the INFERNO aircraft using the aerial refueling capability 22

5.4 Fleet concept of the INFERNO aircraft without aerial refueling 22

5.5 Yearly Fleet concept of the INFERNO aircraft 23

5.6 Drogue-and-probe concept for aerial refueling and maximizing firefighting time 23

5.7 Turnaround drawing 24

5.8 Turnaround time chart 24

6.1 Percentage distribution of the five DOC building costs 25

A.1 Map of the coast scenario A1

A.2 Map of the domestic scenario A1

A.3 Detail steps of the montage A3

A.4 Trend depicting estimated battery specific energy by 2030 at cell-level and pack-level A4

A.5 INFERNO Pilot horizontal FOV A5

A.6 INFERNO Pilot vertical FOV A5

A.7 INFERNO Cockpit: Height in mm A5

A.8 INFERNO Cockpit: Length in mm A5

A.9 INFERNO Cockpit: Width in mm A5

A.10 Static margin for maximum payload A16

A.11 Shift of the CoG for maximum payload A16

A.12 Static margin for ferry range A17

A.13 Shift of the CoG for ferry range A17

A.14 Landing gear requirements A18

A.15 Calculation of turnover angle A19

A.16 Typical equivalent gust velocities for transport aircraft A20

A.17 Drag Polar of the E423M airfoil for Re = 2.5-13 $\cdot 10^6$ and Ma = 0-0.25 . . . . . A21

A.18 Drag Polar of the E545 airfoil for Re = 2.5-13 $\cdot 10^6$ and Ma = 0-0.25 . . . . . A21

A.19 INFERNO at maximum immersion depth A25

List of Tables

3.1 Trade-off study of energy provision concepts 4

3.2 Technical data of INFERNO 5

3.3 TRL of key technologies 5

4.1 GE H85-100 Data 11

4.2 Sion Power Licerion battery properties at cell-level and pack-level for years 2018 and 2022 . 13

4.3 Mass of the individual parts of the aircraft and its lever arms measured from the nose for the calculation of the COG 14

4.4 List of EFIS and IIDS Instruments integrated into INFERNO cockpit 15

4.5 Sensing instruments with dedicated functions enabling 24 h operation capability 16

7.1 Overview of the achieved requirements 25

A.1 Copernicus data for burned area in EU countries (2006 - 2021) A6

A.2 Copernicus data for burned area in Non-EU countries (2006 - 2021) A6

A.3 NCEI data for burned area in USA (2001 - 2020) A6

A.4 INFERNO Operation estimation based on Copernicus data for EU countries A7

A.5 INFERNO Operation estimation based on Copernicus data for Non-EU countries A8

A.6 INFERNO Operation estimation based on NCEI data for USA A9

A.7 INFERNO Fleet annual operation hours estimation A10

A.8 INFERNO Firefighting Fleet annual operation hours estimation A11

A.9 Total LCC and the necessary build-up costs A12

A.10 Calculated DOC and its important parameters A12

A.11 Total gear loads for most-aft and most-forward CoG for initial design A18

List of Abbreviations

AEO	**A**ll **E**ngines **O**perative
AoA	**A**ngle **o**f **A**ttack
APU	**A**uxiliary **P**ower **U**nit
BOM	**B**ill of **M**aterial
CFD	**C**omputational **F**luid-**D**ynamics
CoG	**C**enter **o**f **G**ravity
DOC	**D**irect **O**perating **C**osts
EBIT	**E**xpenditure **B**efore **I**nterest and **T**axes
EDCAM	**E**lectronic **D**isplay for **C**entralised **A**ircraft **M**onitoring
EFIS	**E**lectronic **F**light **I**nstrumentation **S**ystem
EIS	**E**ntry **I**nto-**S**ervice
EO/IR	**E**arth **O**bservation / **I**nfrared
EU	**E**uropean **U**nion
FIRMS	**F**ire **I**nformation for **R**esource **M**anagement **S**ystem
FishBAC	**F**ish **B**one **A**ctive **C**amber
FOV	**F**ield of **V**iew
GE	**G**eneral **E**lectric
GSE	**G**round **S**upport **E**quipment
HUD	**H**eads-**U**p **D**isplay
IIDS	**I**ntegrated **I**nstruments **D**isplay **S**ystem
INFERNO	**IN**telligent **F**ir**E** **R**espo**N**se **O**peration
LCC	**L**ife **C**ycle **C**ost
MPL	**M**aximum **P**ay**l**oad
MTOM	**M**aximum **T**ake-**O**ff **M**ass
MTOW	**M**aximum **T**ake-**O**ff **W**eight
MZFM	**M**aximum **Z**ero **F**uel **M**ass
OEI	**O**ne **E**ngine **I**noperative
OEW	**O**perating **E**mpty **W**eight

OWE	**O**perating **W**eight-**E**mpty
QA	**Q**uality **A**ssurance
SAF	**S**ustainable **A**viation **F**uel
SMA	**S**hape **M**emory **A**lloy
SMP	**S**tandard **M**ission-**P**ayload
STOL	**S**hort **T**ake-**O**ff and **L**anding
TRL	**T**echnology **R**eadiness-**L**evel
USA	**U**nited **S**tates of **A**merica
VTOL	**V**ertical **T**ake-**O**ff and **L**anding

Greek Symbols and Variables

Symbol	Description	Unit
$A_{\mathrm{Inlet,I}}$	Inlet area during immersion	m^2
$A_{\mathrm{Inlet,S}}$	Inlet area of scooping device	m^2
A_{Outlet}	Area of outflow	m^2
A_{Tank}	Cross-section are of tank	m^2
A_{prop}	Area of the vertical propellers	m^2
A	Aspect ratio wing	–
C_{D}	Drag coefficient	–
C_{L}	Lift coefficient	–
C_{L_α}	Lift coefficient gradient	–
D	Drag of the aircraft	N
L_{m}	Length of main landing gear	in
L	Lift of the aircraft	N
Ma	Mach number	–
N_{ENG}	Number of engines	–
N_{OCC}	Number of occupants (crew and passengers)	–
N_{TANK}	Number of fuel tanks	–
N_{c}	Number of crew	–
P_{hov}	Power during hovering	W
P_{Cl}	Power during climb	W
P_{Cruise}	Power during cruise	W
P_{TO}	Power during Take off	W
P_{VTOL}	Power during vertical take off or landing	W
Q_{int}	fuel quantity in integral fuel tanks	gallons
Q_{tot}	total fuel quantity	gallons
Re	Reynolds number	–
SFC	Specific fuel consumption of the aircraft	$\mathrm{g/kWh}, 1/\mathrm{h}$
S_{HT}	Horizontal tail area	m^2
S_{W}	Wing area	$\mathrm{m}^2, \mathrm{ft}^2$
S_{VT}	Vertical tail area	$\mathrm{m}^2, \mathrm{ft}^2$
T_{TO}	Thrust during Take off	N
V_{Kr}	Fuel volume	m^3
V_{LOF}	Lift-off air speed	m/s
V_{Tank}	Tank Volume	m^3
W_{AC}	predicted weight of the AC and anti installation	lbs
W_{AV}	predicted weight of the avionics installation	lbs
W_{CTRL}	predicted weight of the flight control system	lbs
W_{EI}	predicted weight of the engine installed	lbs
W_{EL}	predicted weight of the Electrical System	lbs
W_{ENG}	uninstalled engine weight	lbs
W_{FS}	predicted weight of the fuels system	lbs

Symbol	Description	Unit
W_{FURN}	predicted weight of furnishings	lbs
W_{FUS}	predicted weight of the fuselage	lbs
W_{HT}	predicted weight of HT	lbs
W_{MNLG}	predicted weight of the entire landing gear	lbs
W_{UAV}	weight of the uninstalled avionics	lbs
W_{VT}	predicted weight of VT	lbs
W_{W}	Wing weight	lbs
W_{l}	design landing weight	lbs
W_0	design gross weight	lbs
ΔC_{d}	Difference of drag coefficient of airfoil	–
ΔC_{l}	Difference of lift coefficient of airfoil	–
Λ	Wing sweep at 25% MAC	rad
α	Angle of attack	deg
$\bar{v_{\mathrm{o}}}$	Average outflow velocity	m/s
$\dot{A}_{\mathrm{e}}$	Extinguishing water	$\mathrm{l/s \cdot m^2}$
$\dot{V}$	Flow rate	l/s
ϵ	Glide number	–
$\frac{t}{c}$	Thickness ratio at wing root	–
γ	Flight path angle	deg
λ	Taper ratio of wing	–
μ	friction coefficient	–
ρ	Density	$\mathrm{kg/m^3}$
MAC	Mean aerodynamic chord	m, ft, in
$\mathrm{n}_{\mathrm{lim}_{\mathrm{pos}}}$	Maximum positive load factor	–
ξ_{HT}	Tail dynamic pressure ratio	–
b_{HT}	Horizontal tail span	ft
b_{VT}	Vertical tail span	ft
b	Wing span	m
d_{F}	fuselage max depth	ft
g	gravity constant (9.81)	$\mathrm{m/s^2}$
$h_{\mathrm{I,Depth}}$	Immersion depth	m
h_{w}	Water height in tank	m
h	Height of scooping outlet in tank	m
l_μ	Mean aerodynamic chord	m
l_{F}	fuselage length	ft
l_{HT}	Horizontal tail arm, from wing C/4 to HT	ft
m_{MTOW}	Maximum take-off weight	kg, lbs
m_{fuel}	Fuel mass	kg, lbs
n_{l}	Ultimate landing load factor;$= N_{\mathrm{gear}} \times 1.5$	–
n_{z}	Ultimate load factor;$= 1.5\times$ limit load factor	–
q_{H}	dynamic pressure at max level airspeed	$\mathrm{lbs/ft^2}$
r_{H}	Distance horizontal tail neutral point to CoG	m

Symbol	Description	Unit
r_0	Distance neutral point horizontal tail to neutral point	m
t_{HT}	max root chord thickness of HT	in
t_{VT}	max root chord thickness of VT	in
t_{o}	Time to empty tank by outflow	s
t	Time	s
v_{Flight}	Flight speed	m/s
v_{H}	maximum level airspeed at S-L	KEAS
$v_{\mathrm{o,max}}$	Maximum outflow velocity	m/s
v_{stall}	Stall speed	$\mathrm{m/s}, \mathrm{kts}$
w_{F}	fuselage max width	ft

1 Introduction

The tremendous effects of rapidly spreading forest fires are not only characterized by destroying enormous financial assets but also by endangering people, nature, and society. Reoccurring fatalities among the civilian population and vastly destroyed neighborhoods and habitats emphasize the devastating aftermath of these natural disasters. When global warming and missing rain causes forests to dry out and thus increases the risk of wildfires, a vicious circle resulting in more and larger forest fires is inevitable [1]. While forest fires with particularly devastating dimensions have so far mainly occurred in countries like the USA or Australia, European countries are getting increasingly affected. Examples of these hazards are wildfires fires in Turkey and Greece during the summer of 2021. Even though fighting global warming as a holistic problem has to be seen as the key mission of today's generation, early and intelligent detection of wildfires and effective and quick fire response plays a crucial role while diminishing this hazard [2]. An aerial firefighting operation is especially suitable for this very purpose [3]. Nevertheless, new equipment and vehicles are needed for an increasingly effective, use case oriented fire response in regions affected today and those that will likely be affected in the coming years. The INFERNO team therefore set itself the goal of designing an Advanced Air Mobility firefighting aircraft as part of the DLR Design Challenge 2022 that has the ability to contain the forest fire significantly during the initial attack. This is achieved with a fleet of several aircraft, named after water and weather gods from various mythologies. In addition, it should be possible to take water from smaller natural sources, such as lakes and basins to increase efficiency of the mission. In order to keep production costs as low as possible and to guarantee high utilization rates, a modified version of the aircraft can operate for commercial purposes. Moreover, factors like emissions and noise reduction were considered during development to minimize the environmental footprint of the aircraft. EIS is planned for the year 2030. Based on the analysis of two European forest fire scenarios (cf. chap. 2), chap. 3 explains the selection of the configuration. The individual features are described in detail and the necessary calculations are shown. Aerodynamics and flight mechanics are the first aspects to be considered (cf. chap. 4.1). This is followed by sections describing the propulsion (cf. chap. 4.2), mass calculation (cf. chap. 4.3), cockpit (cf. chap. 4.4) and structural aspects (cf. chap. 4.7). The fleet concept (cf. chap. 5) and the cost calculation (cf. chap. 6) are illustrated in further chapters. Finally, a conclusion is presented.

2 Wildfire Scenarios

An essential part of this year's assignment is the investigation of two additional forest fire scenarios in Europe. NASA's **F**ire **I**nformation for **R**esource **M**anagement **S**ystem (FIRMS) was used for the implementation and data generation as this system reports active fires within a few hours after the first satellite observation occurred. The data comes from MODIS sensors on board NASA Terra, which are analyzed with the help of a fire detection algorithm from the University of Maryland. This ensures a possible detection of fires and thermal anomalies. The sensor resolution is 1 km. The analyzed data is from July 2021. In addition to the severe forest fires in Turkey and Greece, major forest fires raged in Italy and Romania during this period. These two scenarios were chosen because they have a similar magnitude and represent both an inland and a coastal scenario [4], [5].
First, the coastal scenario was considered. The selected area includes the region of Apulia and parts of Basilicata. This corresponds to an area of about 23 000 km^2 with 201 detected fire sources. The highest fire source is at an altitude of less than 500 m above sea level. In this scenario, the airports in Bari and Brindisi would be possible bases. Maps of the forest fire scenarios can be found in app. A.1. In order to analyze the possible benefits of a VTOL capability, the distance to the sea was measured from each fire source in this area. If the distance to a possible inland water source was smaller, the distance to the lake was also measured. The minimum requirement for the lake is a width of 100 m. This limit was set due to the unknown depth of small water sources and the often considerably dried state during the fire season in summer. In 54 cases the sea was the nearest water source and in 147 cases a lake was closer to the fire. The average lake surface is 3.94 km^2. Fig. 2.1 shows that a considerable amount of fire sources is located between 0 and 10 km or 40 and 50 km from the sea. The average distance to the sea is 29.57 km and the maximum distance 62.5 km. Compared to the lakes, it can be seen that a distance between 0 and 20 km is particularly frequent in the coastal scenario. The average distance here is 12.65 km and the maximum distance 42.1 km (cf. fig. 2.2). As a second step, the inland scenario was observed. The selected area includes the districts of Dolj and Mehedinti, which corresponds to an area of about 12 300 km^2. 210 fire sources were detected by the algorithm. The highest fire source is at an altitude of less than 360 m above sea level. A possible base would be Craiova Airport. Here, the same investigations as in the coastal scenario were carried out, whereby the Danube now takes on the role of the sea as it shows similar conditions for scooping. In the inland scenario, the lakes are the closest water source in only 63 cases. The average lake surface is 3.03 km^2. Fig. 2.3 shows that several fire sources are located between 10 and 20 km from the river. The average distance to the river is 16.89 km and the maximum distance 57.89 km. In comparison

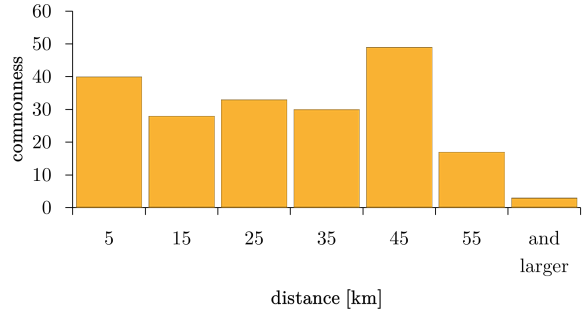

Figure 2.1: coast scenario: distance sea – fire source

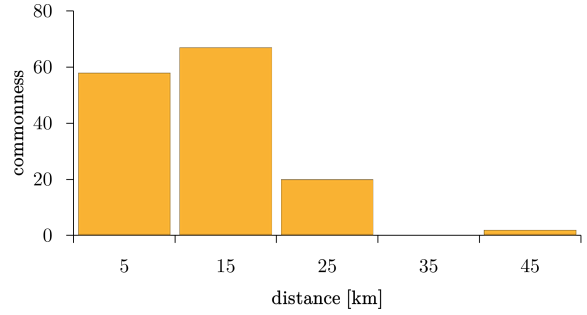

Figure 2.2: coast scenario: distance lake – fire source

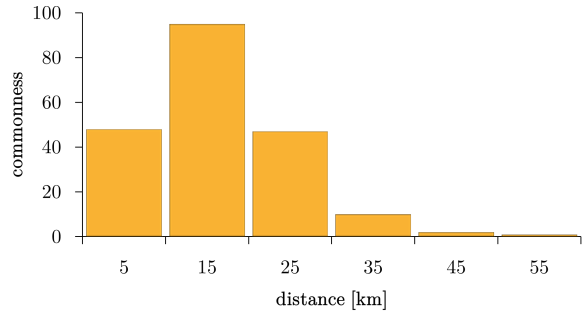

Figure 2.3: Domestic scenario: distance river – fire source

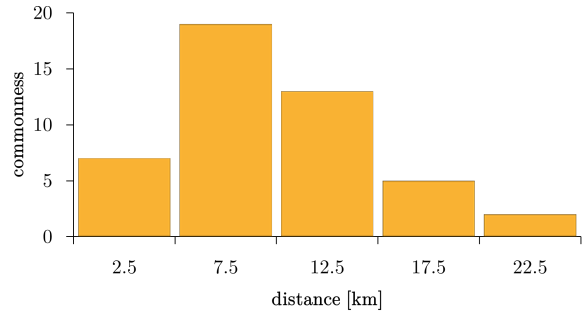

Figure 2.4: Domestic scenario: distance lake – fire source

with the lakes, it becomes clear that a distance between 5 and 10 km is particularly frequent. The average distance is 11.94 km and the maximum distance 28.95 km (cf. fig. 2.4). It can be seen that the advantage of using small lakes is obvious in this scenario and plays a major role for both the coastal and inland areas.

2.1 Initial Sizing – Maximizing Dumped Water

During the preliminary design phase, the optimal range for the aircraft was determined by maximizing the amount of water that is being transported to the fire during a 24 h mission. The total amount of water for one mission is set by the task to 11 000 kg. The amount of transported water during a given period scaled linear with the flight speed of the aircraft. Because INFERNO has many acceleration and deceleration maneuvers during its mission, the cruise speed was set relatively low to 300 km h^{-1}. This is similar to other fire fighting aircraft like the CL-415 (333 km h^{-1}) [6] or the AT-802 (356 km h^{-1}) [7]. For the design mission, the distance between the base and the fire (75 NM) and the water body and the fire (15 NM) was given. In this preliminary design phase, the speed during the flight sections is considered constant and the time for approach, water refilling and take-off at the water body is estimated with 1 min. The turnaround time at the base was set to 5 min. With all these estimates, the water that is delivered to the fire within 24 h depending on the range of the aircraft can be calculated. In fig. 2.5, the amount of water that can be dropped by the fleet of aircraft within 24 h is displayed depending on the range of the aircraft. With an increasing range, the amount ameliorates as expected. The gradient of the graph however significantly decreases at a range of around 1200 km. To achieve an optimal balance between range and therefore fuel volume and a high water transportation rate, the preliminary design range was chosen as 1200 km. Further detailed calculations regarding fuel consumption for this range were performed in chap. 4.2.1.

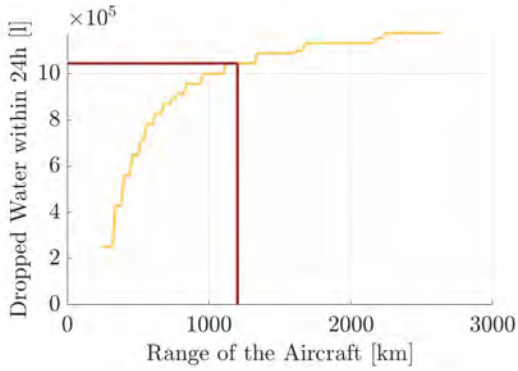

Figure 2.5: Preliminary calculation of the optimal range for water maximization

3 Design Process

In the following chapter, the design process for the INFERNO aircraft is described. Therefore, crucial design decisions concerning the flight capabilities, the energy storage or the overall configuration are presented and justified. Due to the **M**aximum **T**ake-**O**ff **M**ass (MTOM) of less than 5670 kg and a single pilot operation, a certification under EASA CS-23 and FAR Part 23 is seeked.

3.1 Vertical Take-Off and Landing vs. Short Take-Off and Landing

In a first step of the design process, the advantages of a VTOL as well as a **S**hort **T**ake-**O**ff and **L**anding (STOL) were evaluated. The VTOL has the major advantage that no runway is needed for take-off. This means that smaller water surfaces can be used for water refilling. Chap. 2 stated the clear advantage when having the possibility to use smaller water sources in the forest fire scenarios analyzed. In addition, hovering is possible and lower flight altitudes can be achieved. In favor of a configuration with STOL characteristics is the fact that the cruising speed is significantly higher and the payload share in relation to the **M**aximum **T**ake-**O**ff **W**eight (MTOW) is increased. In addition, the power requirement for the same payload is lower than for a VTOL vehicle [8]. This also means that operation and production is cheaper. It is obvious that there are arguments for each of the two concepts. Therefore, the INFERNO team set the design requirement of combining the advantages of both concepts. This is achieved with the help of an electric drive concept, which offers significantly more degrees of freedom in the design of configurations. Due to the small space requirements of electric motors, they can be flexibly positioned or a larger number of small propellers can be used [9]. This leads to improved drive efficiency. Flexible positioning means that swivelling thrusters for vertical take-off and landing can be dispensed, resulting in a significant reduction in maintenance. In addition, a buffer storage allows the power required for short periods to be significantly higher than the available continuous power.

3.2 Fuel Type and Energy Storage Concept

The source of the electrical energy is subsequently examined in more detail. In order to be able to provide the necessary electrical power, various energy storage concepts are available. In the following, four promising methods for energy supply are evaluated:

- Turbogenerator operated with synthetic fuel / kerosene (an internal combustion engine generates shaft power, which is converted to electrical power + buffer battery)
- Turbogenerator operated with hydrogen (an internal combustion engine generates shaft power, which is converted to electrical power + buffer battery)
- Battery (the sole energy storage and power source are batteries)
- Fuel cell (the electric power is produced by a chemical reaction of hydrogen and oxygen + buffer battery)

The comparison is based on six categories (cf. tab. 3.1). Unlike the turbogenerators and fuel cell, the battery does not have to convert the energy to electricity first, therefore it is the most efficient solution. Due to the low gravimetric energy density of current lithium-ion cells compared to kerosene and synthetic fuels and the higher weight of hydrogen tanks compared to conventional integral tanks, the turbogenerator with synthetic fuel or kerosene has the biggest weight advantage. INFERNO is designed to be used on very small rural airstrips that have limited infrastructure and might not have high voltage powerlines or hydrogen infrastructure by 2030. The main goal of the design is it to make INFERNO as versatile and agile as possible. By using synthetic fuel or kerosene and vertical take-off and landing, a base could theoretically be a large plain field with a tank truck for refueling. Thus, the turbogenerator with synthetic fuel or kerosene therefore has a big advantage over batteries and hydrogen. Furthermore it is very well known, has a high technology readiness level (cf. tab. 3.3) and an established supply chain in the aerospace market, which decreases costs and risk during development and EIS. The environmental impact however is due to its consumption of fossil fuels (if fueled with kerosene) or the high energy consumption during the production of synthetic fuel higher than for batteries (that can be recycled [10]) or a hydrogen burning turbogenerator. Because fuel cells do not use combustion, their environmental impact is the lowest. Overall, the dual-fuel turbogenerator powered by synthetic fuel is the most suitable technology for the INFERNO concept and its requirements. It offers the best balance between efficiency, weight, cost and availability. Especially the flexibility in operation with fast refueling, easy availability and transportability of the fuel is a key argument for the use of carbon-based fuel.

	Turbogenerator (synthetic fuel)	Turbogenerator (hydrogen)	Battery	Fuel Cell
Efficiency	0	0	++	+
Weight	+	0	–	-
Infrastructure	++	-	0	-
Costs	+	0	-	–
Environmental impact	-	+	+	++
Technology readiness	+	0	0	-
Result	+4	0	0	-1

Table 3.1: Trade-off study of energy provision concepts; best: ++, worst - -

3.3 Configuration Selection and Key Technologies

To combine VTOL and STOL capabilities, a wing like that of a classic fixed-wing aircraft is indispensable. For the positioning of the wing, a high wing is almost without alternative for amphibian aircraft, as it provides ground clearance and distance to the water during scooping [11]. There were several options for the distribution of the drives, as the electric drives offer substantive flexibility. One option was the usage of tilt rotors but the concept requires more maintenance and is more susceptible to faults and therefore results in more costs. Moreover, the EIS of 2030 has to be considered during the design decisions. Thus, the INFERNO aircraft features separated propulsion systems for both vertical and horizontal flight. As shown in fig. 3.1, the final configuration selection is characterized by 8 VTOL propellers distributed along the wing span to achieve sufficient rotor area. For the positioning of the propulsion, 3 options were investigated. The first option was the positioning at the rear of the tail as a pusher. Moreover, the positioning at the wingtips or classically close to the fuselage was evaluated. The pusher configuration caused ground clearance problems during take-off when the aircraft is rotating conventionally, so it was not suitable for the requirements. When comparing the other configurations, there were advantages for both. However, the advantages of the close-to-fuselage drive, and the associated support of the tail by the propeller wake, outweighed those of the wingtip propellers. When selecting the tail unit, the decision was made in favor of an H-tail unit. Since the rudder area became very large due to the short lever arm and the relatively high wing area, a H-tail has decisive benefits as it divided this area into two separated rudders, thus reducing the height. A more detailed investigation takes place in chap. 4.1.5. Fig. 3.1 and fig. 3.2 show the key characteristics, equipment and technologies of the INFERNO concept. Moreover, the aircraft dimensions are summarized in tab. 3.3 and fig. 3.4, 3.5 and 3.3.

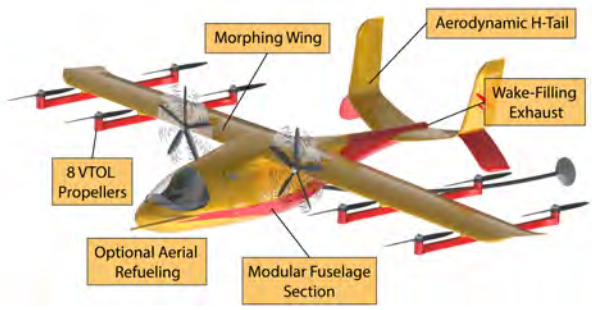

Figure 3.1: Unique characteristics of INFERNO

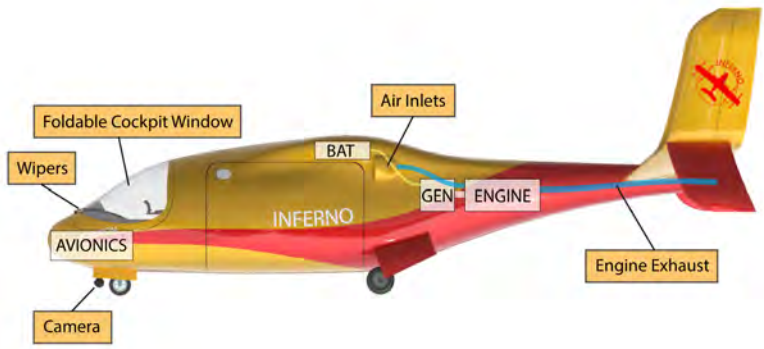

Figure 3.2: Unique characteristics of INFERNO

Aircraft Data	
Length	8.50 m
Height	3.60 m
MTOM	5670 kg
Wing Area	27.4 m^2
Aspect Ratio	9.34
Anhedral	-2°
Sweep Leading Edge	5°
Taper Ratio	0.5
Take-off Field Length	600 m
Climb Rate (hor.)	1400 ft/min
Climb Rate (VTOL)	1000 ft/min
Climb Gradient **A**ll **E**ngines **O**perative (AEO)	max. 20%
Climb Gradient **O**ne **E**ngine **I**noperative (OEI)	6%
Cruise Speed	Ma 0.25
Cruise Altitude	FL 080
Glide Ratio	16.32
Fuel Consumption Design Mission	400 kg

Table 3.2: Technical data of INFERNO

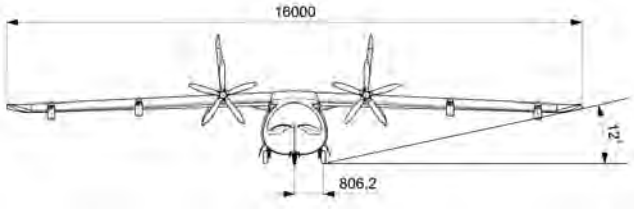

Figure 3.3: Front view of INFERNO

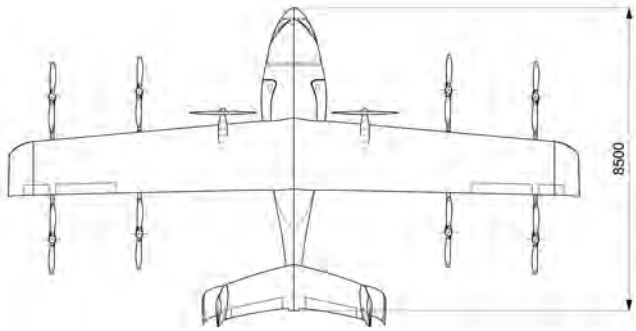

Figure 3.4: Top view of INFERNO

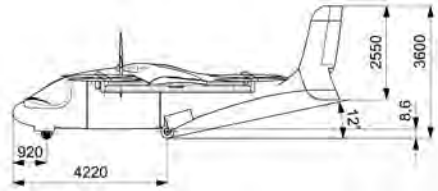

Figure 3.5: Side view of INFERNO

Tab. 3.3 summarizes the key technologies of INFERNO. Additionally, sources are listed for the respective TRLs that show the technical status and further development up to 2030.

Key Technology	TRL
Synthetic fuels	6 [12]
Battery	5 [13]
Wake-Filling	3-4 [14]
Hybrid system	6 [15]
Morphing Wing	6 [16]
Exchangeable fuselage	4 [17]
Electric Motors	4 [18]
Sensing Instruments	6 [19][20]

Table 3.3: **T**echnology **R**eadiness-**L**evel (TRL) of key technologies

4 INFERNO Configuration & Features

This chapter extensively discusses major configuration features as well as further unique selling propositions of the INFERNO concept.

4.1 Aerodynamics and Flight Mechanics

The aerodynamics section covers all relevant design decisions concerning the wing, the empennage and the overall aircraft.

4.1.1 Wing Planform Selection

The general mission design is decisive for the wing planform design. The most important parameter for this is the Mach number. Due to the vertical take-off capabilities, only relatively low cruising velocities can be realized because of the expected drag from the vertical take-off propulsion system. For the targeted cruise speed of 300 km h^{-1}, this means Mach numbers in the range of 0.23-0.25 at 8000 ft. The mission demands good slow flight characteristics, high maneuverability and short take-off and landing capabilities when the aircraft is not started and landed vertically. The decisions for the parameters were made using Roskam's book [11].
The wing loading was chosen in the same order of magnitude as the Canadair CL-415 [6], giving a wingspan of 16 m and a taper ratio of 0.5 with a chord length of 2 m on the wing root and 1 m on the wing tip. This results in a wing area of 27 m^2.
A lower wing loading supports the slow flight characteristics and take-off distances. The 0.5 taper ensures an equally distributed lift over the wing. This taper is achieved in 2 steps. From 2 m chord length on the wing root to 1.5 m at just over 14.5 m span and 1 m chord length on the root tip. Due to the relatively low Mach

numbers, only a small sweep back of the wing is needed. Therefore a decision was made towards a backwards wing sweep of five degrees on the leading edge so that the trailing edge is orthogonal to the fuselage. When it comes to maneuverability in firefighting, on high-wing aircraft, negative dihedral angels of the wing are helping. However, the distance to the water surface when collecting water limits this angle. Thus, an angle of -2° is a compromise for these two boundary conditions. A top view of the wing can be seen in fig. 3.4.

Position of neutral point Determining the position of the neutral point is very important for designing an aircraft. Only when its position is known, the **C**enter **o**f **G**ravity (CoG) can be adjusted so that the static longitudinal stability is ensured [21]. In the determination, it is assumed that the horizontal tail is fixed. Therefore, no change in elevator angle is taken into account. Initially, only the neutral point of the wing-empennage system is considered. The influences of the fuselage or the engines are neglected. The calculation is done as described in app. A.2. In order to refine the results of the simplified neutral point calculation, the influence of the fuselage was subsequently corrected. For this purpose, a method that is common in preliminary design was used [22]. The neutral point of the configuration is at 3.89 m.

4.1.2 Morphing Wing

To optimize the aerodynamics of the aircraft during its agile mission and to fulfill diverse requirements of different flight phases, the INFERNO concept is featuring a morphing wing system. The considered flight phases include rapid climb or descent to deploy or pick up water, short take-off or landing maneuvers as well as slow and high speeds phases. For conventional aircraft, the increase in lift during take-off and landing is realized through high lift devices like flaps and slats. Nevertheless, conventional lift increasing surfaces come with several disadvantages, as high lift devices increase drag by increasing camber. Additionally, noise is increased by multiple separation points on the airfoil near the trailing edge and in the separated zones between flap and wing. A morphing wing concept is diminishing these disadvantages as a smooth and continuous surface can be ensured. Moreover, the need for a high lift coefficient at low speed and a low drag coefficient at cruising speed is combined by the morphing wing technology. Nonetheless, the concept is not applied for the entire wing of the INFERNO aircraft. The wing is still featuring conventional ailerons as morphing ailerons combined with a morphing wing would increase complexity and weight significantly [23]. Thus, the outer area of the wing is using a conventional wing structure combined with conventional ailerons. The INFERNO morphing wing concept is showing differences to previously presented morphing wing designs. The system is variable in thickness over the chord depth having a variable leading edge, active camber and variable thickness, as presented by Coutu et al. [24] and Woods et al. [25], as shown in fig. 4.1. The combination of gas spring actuators which can modify the thickness of the **S**hape **M**emory **A**lloy (SMA) and the variable camber, realized by the **F**ish **B**one **A**ctive **C**amber (FishBAC), provide a fully variable airfoil in thickness and camber. Thereby, 80% of the tendon length is constructed as shown in Couto et al. [24] and the remaining 20% is the FishBAC. This allows differences in $\Delta C_\mathrm{l} = 0.80$.in take-off speeds and at $\alpha = 14°$ and difference in $\Delta C_\mathrm{d} = -0.62 \cdot 10^{-3}$ during cruise and $\alpha = 0°$. This difference in lift coefficient is almost equivalent to a plain or split flap, but without the negative effects normally associated with conventional flaps like stall at lower angles of attack or increased drag or noise.

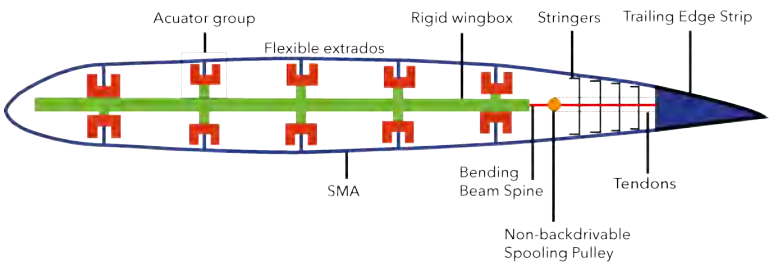

Figure 4.1: Morphing wing system

4.1.3 Airfoil Selection

In general, airfoils are selected according to the time-dominant flight phase. For civil aircraft the dimensioning phase is cruise, whereas for fighter jets this could be dogfight. The INFERNO is operating in several flight phases, as this aircraft performs 17 take-offs and landings in one operational period. Therefore, two flight phases take-off/landing and cruise were chosen for the airfoil selection. Take-off or landing require high lift coefficients, whereas the cruise airfoil must provide sufficient lift and minimize drag. The conducted research included a literature review of existing high lift airfoils and cruise airfoils for low speeds and a comparison through calculations in XFOIL. In the following paragraph, the selected airfoil of the wing and empennage

selection will be described.

Wing Airfoil Selection The large chord depth of the INFERNO and contamination from the environment disturbing possible laminar flow regions must be taken into account. Typically, for high-lift demands the E420 would be better [26] as higher lift coefficients can be obtained, but the E420 loses its high-lift characteristics under high roughness which can be caused by contamination from fire soiling or sprayed (sea-)water. As roughness and Reynolds numbers of up to $Re = 5 \cdot 10^6$ can critically affect the flight properties, the Eppler E423 airfoil was selected. The E423 airfoil is the better choice, as this airfoil can better tolerate these environments [27]. Nonetheless, high-lift airfoils are susceptible to flutter due to their thin character and are generally associated with higher structural masses. To diminish those effects, the E423 airfoil has been modified. The camber was reduced and its relative thickness was increased, as shown in app. A.13. The second chosen airfoil is the E545 Airfoil, which is used in general aviation applications and has an increased laminar bucket and properties which are only marginally affected by increased roughness.

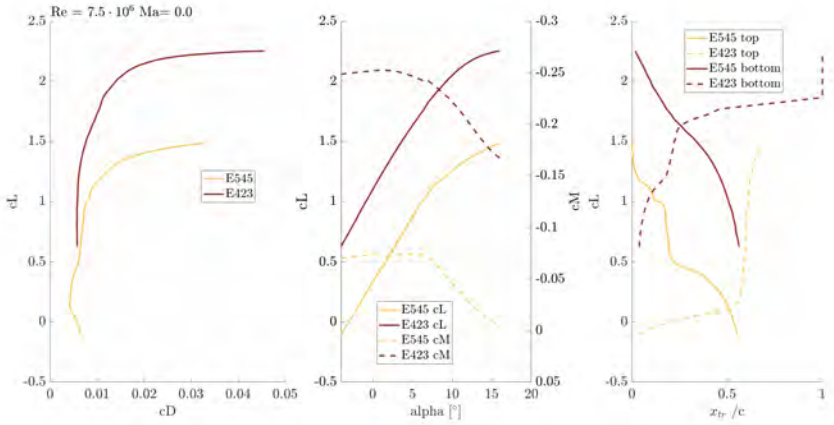

Figure 4.2: Drag polar comparison of E423M and E545 airfoil for $Re = 7.5 \cdot 10^6$

XFOIL was used to analytically calculate the aerodynamic characteristics of the airfoils and to investigate the influence of Reynolds and Mach numbers which vary between $Re = 2.5\text{-}13 \cdot 10^6$ and $Ma = 0\text{-}0.25$ for take-off conditions and cruise speed. Fig. 4.2 show the drag polars of the E 423Modified (E 423M) and E 545 airfoil for the relevant flight phases, as the E 423M will be used for low speed conditions ($Re = 2.5\text{-}7.5 \cdot 10^6$) and the E 545 for cruise phases only ($Re = 7.5\text{-}13 \cdot 10^6$ and $Ma = 0\text{-}0.25$). Switching between airfoils is made possible by the morphing system, which is described in chap. 4.1.2.

Empennage Airfoil Selection Symmetrical airfoils are generally selected for the horizontal and vertical stabilizers [28]. NACA airfoils of the 4-series are therefore used, which have a particularly low drag coefficient. The drag coefficient in a symmetrical airfoil is only influenced by the thickness [28]. As mentioned previously, thicker profiles have less structural mass and are generally more usable to support structures. Therefore, the NACA 0010 airfoil is used for the horizontal stabilizer and the NACA 0008 airfoil for the vertical stabilizer.

4.1.4 Aerodynamic Calculations of the Aircraft

The aerodynamic calculations of the wing were made using AERO Tool, a software tool developed by the IAG (Institute for Aerodynamic and Gas dynamic) at the University of Stuttgart. It uses the panel method to calculate lift and drag of the airfoil. Additionally, it features a XFOIL implementation to calculate the drag. The resulting lift and drag of the wing was calibrated with factors that were obtained from simulating the Airbus A320 as a reference aircraft and comparing the results with the real A320 data. Subsequently, the drag was again calibrated with textbook methods from [29], [30] and [31], to account for the drag of the fuselage. The lift of the fuselage during the flight due to its angle of attack was neglected, because its area is relatively small compared to the wing size. Because of the morphing wing concept (chap. 4.1.2), the airfoil can be changed in-flight. The cruise configuration was simulated using cruise conditions, and the high-lift configuration was simulated assuming approach or take-off conditions. Fig. 4.3 shows the resulting lift to drag ratio in cruise and high-lift wing configuration.

AERO Tool does not return the stall characteristics of the wing and shows convergence problems when the angle of attack causes the flow to separate. Therefore, the graph in fig. 4.3 is interrupted when stall occurs. The wing planform and the resulting local lift coefficient distribution prevents an early tip stall guaranteeing controllability even when the flow starts to separate in the center of the wing. When the aircraft is about to

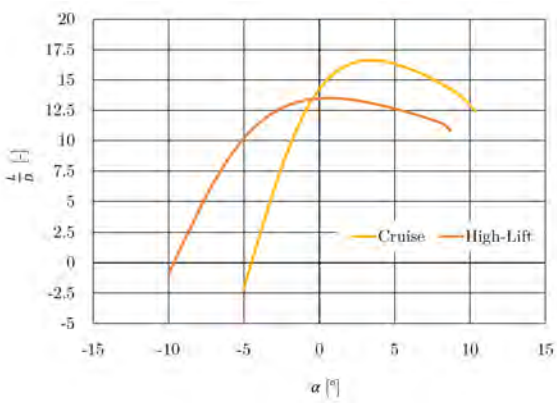

Figure 4.3: Calculated Lift to Drag ratio for Cruise and High-Lift Wing Configuration

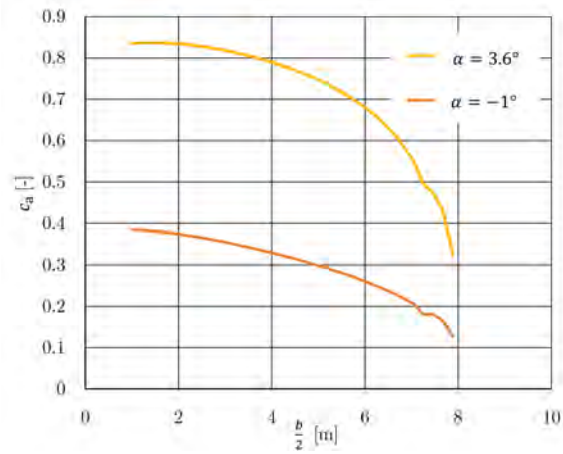

Figure 4.4: Distribution of the lift coefficient for cruise flight with different angles of attack

drop the water, pilot sight is very important, so that the water can be placed as effective as possible, this is achieved by a low angle of attack for cruise flight with payload. At MTOW the angle of attack is about 3.6° and at OWE at about -1° in cruise configuration. This big difference is due to the relatively high payload ratio. Nevertheless, the maximum aerodynamic efficiency stays within this range.
The morphing wing system replaces high-lift devices. The maximum lift coefficient however is not sufficient to do a horizontal take-off with MTOW, this is why the vertical propellers are supporting the take-off and climb at low speeds with high mass.

4.1.5 Tail

The sizing for the vertical as well as horizontal stabilizer is based on volume coefficients which are obtained from literature and comparisons to similar aircraft. Due to a deft positioning of the horizontal propellers, the increase of dynamic pressure at the stabilizers was used to downsize the surfaces.

Horizontal Stabilizer Sizing The size of the horizontal stabilizer S_{HT} is calculated by eq. 1 taken from [32] with $\overline{V}_{\mathrm{HT}}$ as the volume coefficient of the horizontal stabilizer, r_{H} as the distance between the aerodynamic center of the horizontal tail and the center of gravity, S_{W} as the wing area and l_{μ} as the mean aerodynamic chord.

$$\overline{V}_{\mathrm{HT}} = \frac{S_{\mathrm{HT}} \cdot r_{\mathrm{H}}}{S_{\mathrm{W}} \cdot l_{\mu}} \tag{1}$$

The volume coefficient for a flying boat or a general aviation, twin engine aircraft is typically around 0.7 according to [32]. All the other parameters are part of the design and are obtained via iterative calculation. According to [33] the sweep of the horizontal stabilizers ¼-chord line should be a little bit higher than the wing sweep, so that compression effects on the tail occur later than on the wing and in the range of 0° to 35° [32]. In this design 15° for the ¼-chord line and thus 17° for the leading edge is chosen. As the taper ratio 0.8 is chosen, which is a little higher than usual according to [32], but provides us with more space and structural strength for the vertical stabilizer. The calculated area for the horizontal stabilizer would therefore be 6.7m^2. Due to the increase of the dynamic pressure at the stabilizers the size could be reduced by 43% to 3.8m^2. The critical point for the horizontal stabilizer is the go around maneuver, where the propellers deliver 100% thrust. According to [34] the increase in dynamic pressure can be calculated by eq. 2.

$$\frac{q_{\mathrm{H}}}{q} = 1 + \frac{S_{\mathrm{H,Nachlauf}}}{S_{\mathrm{H}}} \cdot \frac{2200 \cdot P_{\mathrm{av}}}{\frac{\rho}{2} \cdot v^3 \cdot \pi \cdot D_{\mathrm{P}}^2} \tag{2}$$

The dynamic pressure at the horizontal tail during go around increases therefore nine fold, that is why the reduction of horizontal tail size is permissible. According to [29] the elevators are about 25% of the horizontal tail area and have a constant percent chord for structural reasons. Due to the vertical tail being directly connected to the horizontal tail, the horizontal tail is fixed and the trimming is done via the elevators.

Vertical Stabilizer Sizing As the horizontal stabilizer, the size of the vertical stabilizer S_{VT} is determined also by its volume coefficient $\overline{V}_{\mathrm{VT}}$ the distance between the aerodynamic center of the vertical stabilizer and the COG r_{V}, the wing area S_{W} and the wingspan of the wing B_{W} and can be calculated with eq. 3 from [32].

$$\overline{V}_{\mathrm{VT}} = \frac{S_{\mathrm{VT}} \cdot r_{\mathrm{V}}}{S_{\mathrm{W}} \cdot l_{\mu}} \tag{3}$$

The volume coefficient is derived from literature like [29] and chosen as 0.06. The total area of the vertical stabilizer would therefore need to be 6 m^2. The vertical stabilizers face an increase dynamic pressure by the propellers as well and therefore the size can be reduced, which also decreases drag. The vertical stabilizers face the highest loads, when one engine fails. The increase in dynamic pressure due to the propellers can be calculated with eq. 2 again. The increase in dynamic pressure is lowest when one engine fails during cruise flight. Furthermore only one engine is operative in this scenario, so only one vertical tail faces the 44 % increase in dynamic pressure. This allows, to decrease the vertical tail area by up to 22%. A vertical tail area of 4.9m^2 is chosen, which is a 18% reduction.
The wing sweep of the leading edge is chosen as 12°, which is in the typical range of 0 to 55 °[32]. The resulting wing sweep of the 1/4-chord is 11°.
According to Raymer [29], the control surfaces are about 32% of the total vertical stabilizer area. 40% of the airfoil chord was dedicated to the rudder surface in the upper part of the vertical tail, so that the lower part is free of moving parts, which makes manufacturing and maintenance easier and cheaper. The detailed sizing of both the horizontal and vertical stabilizer can be seen in fig. 3.4.
Because INFERNO has two vertical tails, there are no special requirements regarding spin recovery. To avoid high mach numbers and therefore high drag in the area, where the vertical and horizontal tail are joined, the position of maximum thickness of the horizontal and vertical tail does not match. Fig. 4.5 depicts that there are no angles that are smaller than 90°in order to keep the inference drag as low as possible.

Figure 4.5: Tailplane arrangement with no angles smaller than 90° for lower interference drag

4.2 Propulsion and Battery

The VTOL and conventional option for take-off and landing leads to increased demands on the powerplant and engines. In the following chapter, the power demand is discussed and the selected hybrid configuration and energy management system is presented.

4.2.1 Calculation of Power Demand

This calculation of the power demand in the various flight phases form the basis for the subsequent sizing of the powertrain. All calculations were done according to "Flugzeugentwurf I" by Prof. Strohmayer [32], "GENERAL AVIATION AIRCRAFT DESIGN: APPLIED METHODS AND PROCEDURES" by Gudmudsson [35] and "Grundlagen der Hubschrauber Aerodynamik" by van der Wall [36] for vertical flight. The formulas that were used during the various flight phases can be found in app. A.8. For all propellers a propeller efficiency of 85% ([35]) and an electric motor efficiency of 95% ([37], [38]) was estimated.
In operation, the vertical propellers can be used during take-off as well. With intelligent thrust vectoring, the required down force at the horizontal tail can be reduced. The effects of this on the wing aerodynamics however need further and more test and detailed **C**omputational **F**luid-**D**ynamics (CFD)-Simulation. In Fig. 4.6 the power demand is displayed for horizontal and vertical flights. The power demand decreases over time, because the aircraft gets lighter after it burns the fuel. This could also be used to increase the amount of water that is being scooped from the water body. Measuring this however is very difficult and should only be done, when enough operational experience with the aircraft is gathered. Furthermore it can be seen, that the vertical take-off and landing consumes way more power than the horizontal flight. Therefore the maximum amount of water, that can be carried during these flight phases is limited to 2000 kg.
Depending on the distance between the base and the fire, and the fire and the water body, it can be more

efficient to start at the base with empty water tanks. In the design mission, this could safe up to 24 kg of fuel. But because at wild fires, the time until the first attack is crucial, the aircraft was filled with water at the base.

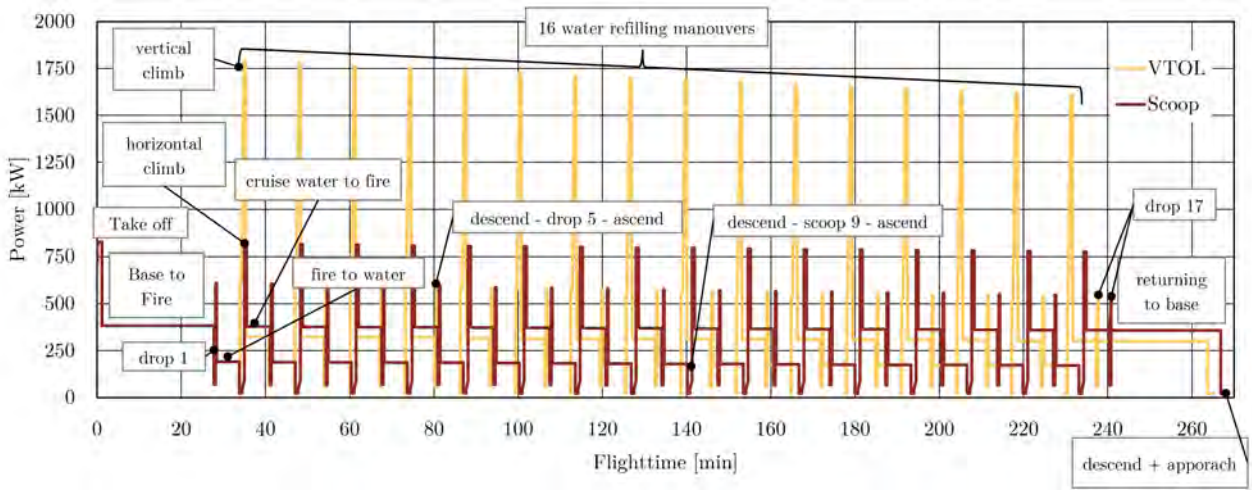

Figure 4.6: Power demand for the horizontal and vertical propellers during horizontal and vertical flight

Transition between Vertical and Horizontal Flight
One of the most critical flight phase is the transition between vertical and horizontal flight. In order to safe fuel, the transition should be done as low as safely possible. In this phase, the morphing wing has its high-lift profile and hovers with its vertical propellers. Fig. 4.7 shows the power demand during the transition between vertical and horizontal flight.
The limiting factor is the maximum of 1800 kW electrical power that the powertrain can provide (1200 kW from the battery and 600 kW form the engine). The horizontal propellers use the excess power, that is not used by the vertical propellers to accelerate the aircraft. With higher speeds, the wing generates more lift and the power at the vertical propellers can be reduced. After approx. 11 seconds, the wing generates enough lift to turn off the vertical propellers. They are then locked in an aerodynamic optimal position for horizontal flight. With further acceleration, the angle of attack is reduced and then the profile of the morphing wing is slowly changed into cruise configuration to enable efficient cruise flight.

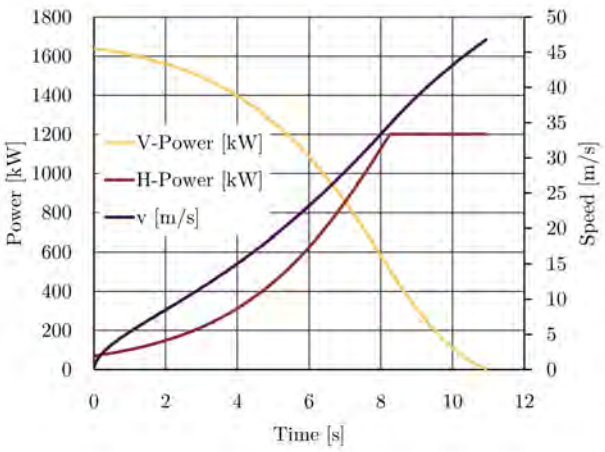

Figure 4.7: Power demand during transition between vertical and horizontal flight

4.2.2 The Hybrid Configuration

Due to the VTOL capability, surges in the power demand occur, which last only for a short amount of time (less than one minute). Furthermore, INFERNO has more propellers than on a conventional airplane (eight motors for vertical take-off and two for horizontal flight). Both of these factors are ideal for installing a hybrid energy system.
Fig. 4.8 shows a schematic overview of the energy system being installed in the aircraft. The eight propellers for vertical flight are powered by 250 kW electric motors, and the two propellers for horizontal flight use a 600 kW electric motor each. In the middle of the wing, the 60 kW h battery pack is placed (cf. chap. 4.2.5). Behind the payload module, the generator and the power electronics are installed. The generator is directly powered by the turbine engine (cf. chap. 4.2.3). Due to the redundant energy system from the relatively high capacity battery and the turbine engine, no **A**uxiliary **P**ower **U**nit (APU) was installed.

4.2.3 Powerplant Selection

The best and most efficient choice of powering an aircraft of up to 300 km h^{-1} are turboprops. Turboprops allow high power-to-weight ratios without losing most of their power at high altitudes. While piston engines would also be a suitable selection for low speeds, they are not designed for high altitudes and the shaft rotational speeds are too low to adequately power a generator.
The INFERNO is powered by the **G**eneral **E**lectric (GE) H85-100 referenced as H85, as it is an optimal engine for all flight conditions. The H85 can use biofuels, also known as **S**ustainable **A**viation **F**uel (SAF)[39]. Moreover, the H85 offers enhanced electronic engine and propeller control, which increases efficiency of the engine [40]. Additionally, turboprops allow excellent connection to power generators for a hybrid electric system, as described in chap. 4.2.2 and fig. 4.9, due to their high rotational speeds as present in other gas turbines. The SFC of the engine is estimated to be similar to other comparable engines like the GE-Catalyst, that offers a SFC of less than 300 $\frac{\text{g}}{\text{kW}}$ [41].

Figure 4.8: Illustration of the hybrid energy storage system

Engine Data	H85-100
Overall length [mm]	1675
Overall width [mm]	590
Overall height[mm]	650
Dry mass [kg]	200
Maximum continuous power at sea level [kW]	634
Specific Fuel Consumption[g/kWh]	<0.3

Table 4.1: GE H85-100 Data [43]

4.2.4 Propeller and Electric Motor Selection

When selecting the propeller, it was decided to use products that are already available on the market. This brings advantages in terms of costs and availability. For the horizontal propulsion, the aircraft use two 5-bladed MTV-27 from MT-Propeller with a diameter of 82.7 in [44]. For the vertical lift, it features eight 2-bladed MTV-20 with a diameter of 200 cm [45]. Both types of propellers are constant speed propellers with variable pitch. The MTV-20 operates at 2700 rpm and the MTV-27 at 2200 rpm. The MTV-20 propellers are not specifically designed as lift propellers, because usually specific rotor blades are designed for the different types of helicopters and their missions as they strongly influence the drag in forward flight. The propeller profiles could, however, be exchanged or optimized at a later date if necessary. No specific product was selected for the electric motors. There are already electric motors in the required power classes, but not yet optimized for aviation. However, with Wright Electric [18], a development is underway that aiming to introduce electric motors for aviation from 500 kW to 4 MW power and a power-to-weight ratio of 10 kW kg^{-1} by 2026 [18]. A 2 MW motor is already in the testing phase. Since this company is working with major partners such as NASA, it is likely that the availability by 2030 is ensured. For the volume calculation and reference product sheets from existing motors of the company YASA were used [46].

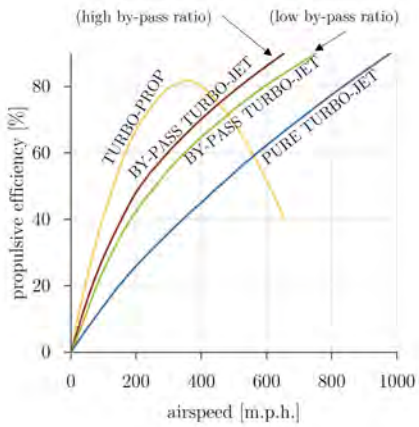

Figure 4.9: Propulsive efficiency comparison for various gas turbine engine configurations according to [42]

4.2.5 Battery Sizing

At the start of the battery sizing process, several feasibility factors in the form of requirements for the battery concept were defined. These factors pertain mainly to the in-flight energy consumption demands of the electric motors during VTOL and SCOOP manoeuvre and are listed as following:

- Available installation space and mass budget constraints
- Battery capacity: 60 kW h
- High specific energy and energy density
- Very high charge-discharge rate (C-Rate)
- Market availability
- Operational life (cycles)

Initial power consumption calculations, during all different flight modes, with a 60 kW h battery pack concluded maximum required electrical power $P_{\mathrm{E}_{\max}}$ at 1238.39 kW_e. The integrated battery pack, as mentioned earlier, shall sustain $P_{\mathrm{E}_{\max}}$ for an approximated 1 min duration of VTOL / SCOOP, for which, the required maximum C-Rate of 20C was calculated. An off-the-shelf battery pack with 20C discharge rate and a considerably high specific energy is still a few years ahead in the future. Therefore, as an initial practical approach to the sizing process, the calculations defining the battery dimensions were executed by developing a conceptual battery pack using the commercially available Sion Power Licerion® High Energy Density Cells. The design properties of individual Licerion® pouch cells are presented in tab. 4.2. The cell's parametric behaviour across multiple C-Rates is represented in fig. 4.10 adapted from [47], wherein at cell-level, the approximated values for specific energy and energy density at peak power consumption are 340 $\mathrm{W\,h\,kg^{-1}}$ and 560 $\mathrm{W\,h\,L^{-1}}$ respectively. These values are further used for determining the mass and volume of the cells that are to be integrated into the battery pack. The theoretical cumulative volume of the cells in the INFERNO battery pack was calculated to be approximately, 107 L and the approximated cumulative mass was calculated as 176 kg. The total battery pack mass also comprises a mass build-up factor that takes into consideration the mass of battery casing, battery management system, wires, and the battery pack's thermal management system [48]. Adapted from [48] and also confirmed in a brief conversation with a Sion Power battery engineer, a mass build-up factor of 1.4 was approximated for determining the energy and physical properties of the pack at battery-level. The total battery pack mass and volume were calculated to be 246 kg and, 150 L respectively. Tab. 4.2 gives a detailed overview of the relevant properties at cell-level and battery-level.
Ongoing research at Sion Power in 2018 estimated new Licerion® technology in 2022 to have significantly improved overall properties at cell level. The 2022 awaited Licerion® cells with a nominal specific energy and energy density of the 650 $\mathrm{W\,h\,kg^{-1}}$ and 1300 $\mathrm{W\,h\,L^{-1}}$ respectively, could lead to a (nominal) theoretical battery mass of as low as 129 kg and a theoretical volume of 65 L respectively, resulting in a better fuel economy, increased operation life and payload capability. At peak power consumption (20C) assuming 75% energy capacity delivery, the mass, and volume at battery-level are presumed to be at 185 kg and 92 L respectively [47]. The 2018 battery-level physical properties protrude over the mass budget restrictions and the 2022 battery-level values are significantly lower in comparison, but still slightly exceed the desired mass budget. A literature report on battery advancement trends made available by NASA shows that the specific energy of a cell at 270 $\mathrm{W\,h\,kg^{-1}}$ in 2018 could be projected at 690 $\mathrm{W\,h\,kg^{-1}}$ by 2030 with an annual increase rate of 8% at cell-level [49]. A similar trend, with an 8% annual increase rate, extrapolated for the 2018 Licerion® technology with current 340 $\mathrm{W\,h\,kg^{-1}}$ estimates the cell-level specific energy to be 856 $\mathrm{W\,h\,kg^{-1}}$ and 582 $\mathrm{W\,h\,kg^{-1}}$ at battery-level (32% loss from cell to pack) by 2030 with the battery pack weighing just about 103 kg. In order to keep the battery pack out of the critical component's list for the EIS and to account for additional fasteners and cables, the battery pack was estimated at 400 $\mathrm{W\,h\,kg^{-1}}$, which leads to a gross mass of 150 kg. At EIS, this relaxed requirement can lead to a cell with higher cycle life or more cells, which leads to a lower C-Rate and thus improves cycle life as well [50].

4.2.6 Fuel Tank Sizing

In chap. 4.2.1, the amount of fuel required for the design point was calculated. In order to verify whether the space provided for fuel in the outer area of the wing span is sufficient, the tank volume is estimated. For this purpose, a statistical procedure according to Torenbeek [30] is used for the preliminary design. This will have to be reviewed at a later stage of development. In order to take into account the installation space used by the battery, the calculation is carried out with the aid of a comparative wing, which only represents the outer 6 m of the half-span. It was assumed that no fuel can be accommodated in the winglets. Using eq. 4, this results in

a maximum tank volume of 1391 L.

$$V_{\mathrm{Kr}} = 0,54 \cdot \frac{{S_{\mathrm{W}}}^2}{b} \cdot \left(\frac{t}{c}\right)_{\mathrm{i}} \cdot \frac{1+\lambda\sqrt{\tau}+\lambda^2\tau}{(1+\lambda)^2} \qquad \text{with} \quad \tau = \frac{\left(\frac{t}{c}\right)_{\mathrm{a}}}{\left(\frac{t}{c}\right)_{\mathrm{i}}} \tag{4}$$

The calculated value was reduced by 30% to ensure the needed space for the morphing wing's actuators (cf. subsubsection 4.1.2). The maximum available fuel volume is therefore 974 L, which corresponds to 780 kg of JET A-1 ([51]). The additional available fuel can be used for air refueling, as explained in subsubsection 5.2.4.

4.2.7 Engine Air Intake and Exhaust

The engine is supplied with air from both sides via air intakes see fig. 3.1. They are positioned high enough to prevent splash water from getting in. Unlike other aircraft, the exhaust gases are not discharged directly behind the engine out of the air frame, but are routed to the rear through the tail boom, where they flow out. The air flow is also shown in fig. 3.2. The exhaust gas flow is used to reduce the drag of the fuselage via wake filling, which is currently the subject of research. The CENTRELINE project [52] is investigating the possibility of increasing efficiency by introducing additional energy centrally at the tail. One of the findings is, that not too much thrust in relation to the total thrust is required to reduce fuselage drag significantly [53]. Even though INFERNO only uses the exhaust gas with its residual energy for Wake Filling, a noticeable drag reduction should be achieved. For detailed predictions, extensive CFD simulations are required. The exhaust pipe is made out of heat resistant materials, like nickel-chromium alloys [54]. Because the exhaust gas is discharged in the rear, the tailboom faces no hot exhaust temperature from the outside, like it would, if the exhaust gas is blown out closer to the engine. The CENTRELINE project is scheduled to have a EIS until 2035. However, INFERNO's wake filling is not of this magnitude and does not use an extra propulsion unit at the rear but only uses the remaining energy of the exhaust gas. Therefore technical maturity should be given until 2030.

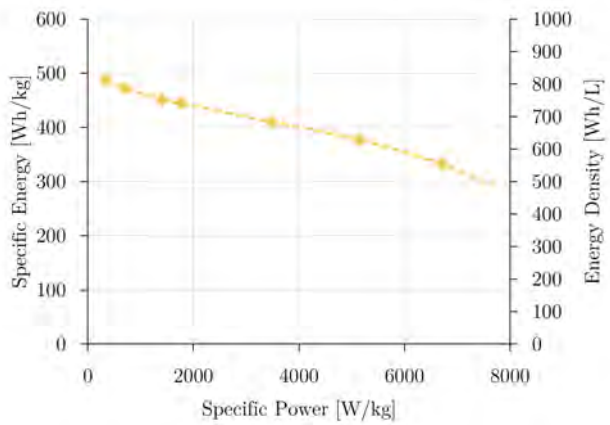

Figure 4.10: High power Licerion® cell energy across different C-Rates according to [47]

4.3 Mass Calculation and Balance

The calculation of the mass of the individual components is the basis for the calculation of the **O**perating **W**eight-**E**mpty (OWE) and the CoG. There are different methods for determining the mass of the individual components. In this report, the method according to Gudmundsson / Nicolai is used [35]. This method is based on a series of statistical equations. The equations for the calculation of the individual component masses can be taken from app. A.9. In order to optimize the results, calibration was performed with two reference aircraft (Cessna 404 and AK 4). For this purpose, the masses of the reference aircraft were first calculated using the same formulas followed by the determination of calibration factors using the known masses. However, those factors produced implausible results because both aircraft are heavily different in size compared to INFERNO. The component masses of a similar aircraft were not known. Thus, a plausible calibration was not possible. The results of the calculation can be found in tab. 4.3. Nikolai's eq. 34 only calculates the mass of the entire

	Build-Up Factor = 1.4*			
	Cell-Level		Battery-Level	
Properties (at 20C)	2018	2022	2018	2022
Specific Energy [Wh/kg]	340	455*	244*	324*
Energy Density [Wh/L]	560	910*	400*	652*
Unit Mass [kg]	176	132*	246*	185*
Unit Volume [l]	107	66*	150*	92*

Table 4.2: Sion Power Licerion battery properties at cell-level and pack-level for years 2018 and 2022 [47]; * represents mathematically / scientifically backed presumptions

	Mass [kg]	Lever Arm / COG [m]
Wing	508.4	4.2
Fuselage	229.2	3.0
Vertical Tail	29.6	8.4
Horizontal Tail	46.3	7.8
Main Landing Gear	22.5	4.5
Nose Landing Gear	11.3	0.9
Electric Engines	470.8	3.7
Fuel System	36.0	3.3
Flight Controls	179.8	3.0
Engine & Generator	265.7	5.6
Electrical System	105.7	3.8
Avionics	102.9	0.2
Air Conditioning and Anti-Ice	107.8	1.8
Furnishings	44.4	1.3
Batteries	150.0	3.8
Operator Items / Pilot	100.0	1.0
OWE	**2410**	**3.8** (26%MAC)
Fuel	460	3.6
Water / Flame Retardant	2800	3.2
MTOM	**5660**	**3.5** (7%MAC)
Maximum Zero Fuel Mass (MZFM)	**5410**	**3.7** (20%MAC)

Table 4.3: Mass of the individual parts of the aircraft and its lever arms measured from the nose for the calculation of the COG

landing gear. However, For the CoG calculation, it is important to have separate masses for the nose and main landing gear. The share of the nose landing gear on total landing gear mass was estimated to be 1/3 and the share of the main landing gear 2/3 respectively.
The mass of some critical components was estimated more thoroughly. Because an existing engine was used, the engine mass of the uninstalled engine was known as 200 kg (cf. chap. 4.2.3). Furthermore, the estimated mass of the uninstalled generator is 7 kW kg^{-1} (including Power Electronics) ([55], [56]), with a 600 kW Generator, this leads to a mass of 85 kg. The specific energy density of the electric motors was estimated with 12 kW kg^{-1} (cf. chap. 4.2.4 and chap. 4.2.5 for the the determination of the batteries mass).
In order to determine the aircraft's CoG, the position of the individual components is required in addition to the individual masses of the components. A detailed design must be available for this purpose (cf. fig. 3.5). The static margin is in the range of 5.7% to 25.4% of the reference wing length. The maximum shift of the COG during a load case is less than 18 percentage points of the reference wing length. Fig. 4.11 and 4.12 show the required diagrams of the static margin and the absolute position of the CoG in respect to the MAC for **S**tandard **M**ission-**P**ayload (SMP). In the app. A.10 the same diagrams are shown for **M**aximum **P**ay**l**oad (MPL) and the ferry range. As seen, the required static margin can be maintained during the entire mission.

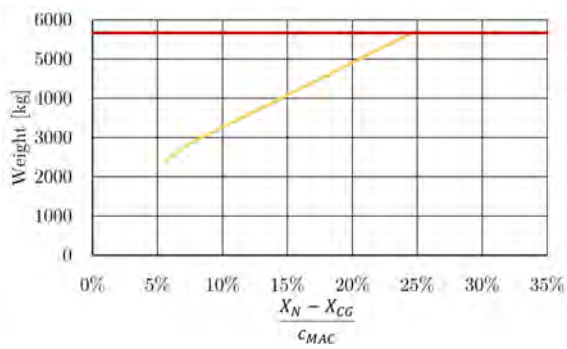

Figure 4.11: Static Margin during water and fuel loading with respect to the MAC in the Design Mission

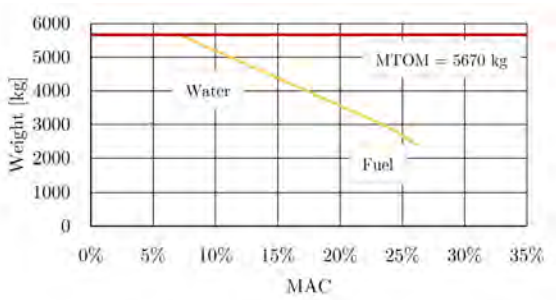

Figure 4.12: Shift of the CoG during water and fuel loading with respect to the MAC in the Design Mission

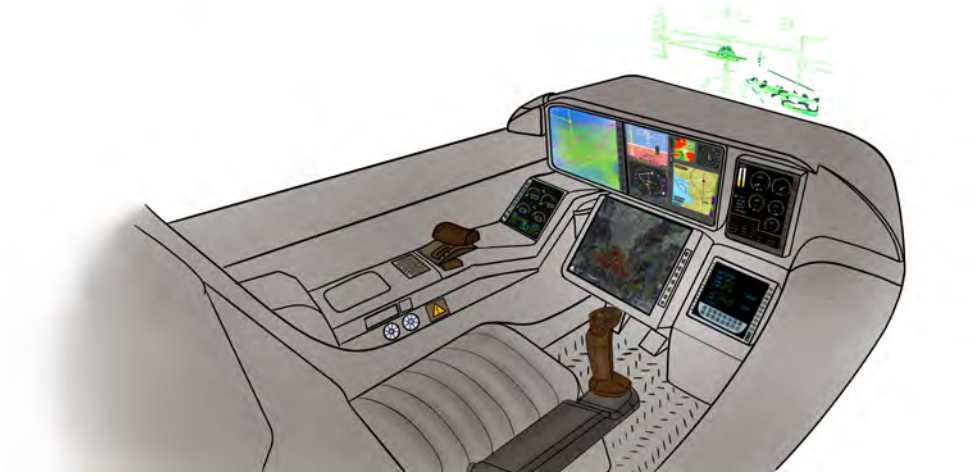

Figure 4.13: INFERNO cockpit design concept with integrated instruments from tab. 4.4

4.4 Cockpit

The cockpit design described in this section is an early approach to an ergonomic and operation centered single pilot cockpit concept for INFERNO. Current parameterisation of the INFERNO glass cockpit focuses more on a pilot workspace and the necessary instruments. The cockpit dimensions are 1169 mm × 1663 mm × 1436 mm (H × L × W) and comprises a 592 mm × 989 mm (H × L) flight deck consisting of 6 displays dedicated to **E**lectronic **F**light **I**nstrumentation **S**ystem (EFIS), an **H**eads-**U**p **D**isplay (HUD) and for the **I**ntegrated **I**nstruments **D**isplay **S**ystem (IIDS) an **E**lectronic **D**isplay for **C**entralised **A**ircraft **M**onitoring (EDCAM). A detailed overview of the electronic displays and their functions are illustrated in tab. 4.4 below.

Human factors have a huge impact on the psychology, physiology, and the awareness of the pilot [62]. The cockpit employs intuitive control elements such as verbal and mechanical outputs to confirm pilot commands. Several other features such as an alerting system for emergency indication, LCDs to maintain 'static dark' ambiance and larger touchscreens for effective human-machine interaction bring an increased guidance and control to the cockpit. Larger synthetic vision touchscreens also lead to consistent luminance, increased readability, larger **F**ield of **V**iew (FOV), increased situation awareness and uninterrupted operation during instrument flight

Category	Instrument	Function	Count
Electronic Flight Instrumentation System (EFIS)	Primary Flight Display (PFD)	3-D Terrain, approach guidance, Enroute, terrain alerting, visual runway, mission manager [57], [58]	1
	Multi-Functional Display (MFD)	Navigation, flight planing, digital (night mode) charts & graphs, synoptics, audio & radio management, checklist [58]	2
	High-Res Liquid Crystal Display	Colour & IR imagery from camera, cockpit browser, meteorological data, clock, etc.	2
	Multi-Functional Radar Display (MFRD)	Weather radar, Terrain, Traffic, Lightning, flight management and navigation system [59]	1
	Heads-Up Display (HUD)	Altitude, airspeed, horizon line, slip/skid and turn/bank indication and heading [60]	1
Integrated Instruments Display System (IIDS)	Electronic Display for Centralised Aircraft Monitoring (EDCAM)	Primary engine indications, fuel quantity, flap and slat position, warning & caution alert, system synoptics, permanent flight data [61]	1

Table 4.4: List of EFIS and IIDS Instruments integrated into INFERNO cockpit

conditions [63]. The displays also have integrated controller consoles for touchscreens and HUD as an alternative to navigating the displays via touch in turbulent conditions. The integrated seat is adjustable to accommodate a range of pilot dimensions, and the seat positioning also enables a primary horizontal and vertical FOV of the flight deck very well within the defined requirements in [63]. A preliminary 3-D design of the cockpit with relevant dimensions is attached in app. A.5.
For a continuous day and night fleet performance of the INFERNO aircraft, ease of accessibility to the primary control instruments, display panels and hand consoles are important to cockpit design efficiency. The pilot governs the sidestick with the right hand and controls the throttle with the left. A preliminary 2-D design of the INFERNO cockpit is depicted in fig. 4.13. A geometric model and layout simulation of the cockpit can further be realized using the ParaPy [64] platform at a later stage in design wherein, multiple other factors such as the design eye reference point, pilot posture, comfort angles, and flight deck detailing could further be explored.

4.5 Sensing Instruments

A task as challenging as aerial surveillance and suppression of wildfires requires tackling of several simultaneous scenarios mid-air. A pilot during his/her operation depends on visual aids and live reports from the ground operators. It is necessary that the pilot from the INFERNO cockpit is able to read into the surroundings and has the latest events communicated. INFERNO employs a state-of-the-art set of sensing instruments that shall enable the pilot to operate efficiently for a continuous 24 h day and night mission period in terms of firefighting. The aircraft is equipped with an **E**arth **O**bservation / **I**nfrared (EO/IR) surveillance system, which allows the pilot to visualize the wildfire scenario during day and in darker hours. The infrared also helps the pilot see through the inevitable smoke clouds. The real-time video feed can be visualized on any of the two LCDs on the flight deck. The communication aspect is covered by a multi-functional hybrid aircraft tracking and communication device, and a real-time update on meteorological factors shall be provided by a weather surveillance radar. For a 3-D mapping of the terrain below, an airborne laser scanner could also be integrated into the aircraft's belly with a few minor design changes. The sensing instruments and their detailed functionalities are vividly detailed in tab. 4.5 below.

Instrument	Function
EO/IR surveillance system	Gyro stabilized thermal & daylight camera, laser rangefinder, onboard low-light & image blending, real-time heat map & temperature profiling, GPS [65], [66]
Weather surveillance radar	Real-time meteorological data, detection of hazards and debris
Satellite and cellular hybrid aircraft tracking and communication device	Flight data recording & monitoring, data offload, internet access, satellite & cellular voice calls, continuous satellite & cellular tracking [20]
Airborne laser scanners *	Quick & precise high altitude 3D-Scan, ground vegetation mapping, forest height & density recognition [19]

Table 4.5: Sensing instruments with dedicated functions enabling 24 h operation capability (* indicates optional but feasible technology)

4.6 Water Pick-Up and Dropping

As wildfires spread rapidly in time and space, it is critical for any aerial firefighter to pick up water in the shortest time possible. In addition, certain water collection methods are restricted in space as these require particularly large amounts of space, such as scooping. In the following chapter, two water collection methods are presented that are installed in the INFERNO, scooping and intake via immersion. Afterwards, the water-release system is described.

Scooping Scooping is a well known and proven method which is already used in the Canadair aircraft, such as the CL-415. In scooping, a water source is overflown and an inlet is submerged, as the forward movement in flight collects water by means of dynamic pressure. The INFERNO has two inlets, which allow lower momentum forces and quicker refilling of the water tank as the refilling of the water tank with a single inlet would be retarded due to baffle plates in the tank. With scooping, in contrast to immersion, the entire tank can be filled.

The aircraft will scoop with a speed of v_{Flight}=30 m s^{-1} and a total inlet area of $A_{\text{Inlet,S}} = 0.015\,\text{m}^2$. The tank capacity is $V_{\text{Tank}} = 3\,\text{m}^3$ and the outlet to the tank is at a height of $h = 3\,\text{m}$.

$$v_{\text{Inlet,Tank}} = \sqrt{v_{\text{Flight}}^2 - 2gh} \tag{5}$$

This results in the flow rate and the time to fill the tank.

$$\dot{V} = v_{\text{Flight}} \cdot A_{\text{Inlet,S}} \tag{6}$$

$$t = \frac{V_{\text{Tank}}}{\dot{V}} \tag{7}$$

Based on these formulas, the distance to fill the tank is calculated to be 207 m and the tank is filled in a time of t=7 s.

Immersion The process of immersion is generally used by helicopters carrying large water buckets. These buckets create a large amount of drag and can be dangerous, as helicopter pilots have to estimate the distance between buckets and ground objects and avoid entangling with static ground objects. Therefore, moving the bucket into the fuselage or utilizing the fuselage as a bucket negates both disadvantages. Additionally, immersion takes a fraction of time of conventional water pick-up methods and small bodies of waters or medium-heavy seas can be approached. The immersion process starts by approaching any body of water and slowly descending near surface level. Then two flaps on the underside of the fuselage are opened, and the horizontal propellers completely halt, only the vertical propellers are operating. Slowly, the fuselage is submerged to a depth of $h_{\text{I,Depth}}$=0.8 m as illustrated in app. A.14. After reaching the desired depth, the flaps on the underside of the fuselage are closed together with the venting and refilling valves in the upper tank area. The vertical propellers start running at full power until an altitude appropriate for the pilot is reached. Meanwhile, the horizontal propellers start until a safe speed is reached for the VTOL propellers to be shut off.
The inlet area for the immersion process is set at $A_{\text{Inlet,I}}$=0.4 m^2 and the tank is filled to a volume of 2.5 m^3. As the aircraft descends with a velocity of 1.11 m s^{-1}, to prevent any unsettling of the pilot or aircraft, the depth of immersion of 0.8 m is reached in 1.4 s. The average area of the tank is A_{Tank}=2.78 m^2 and the time to fill the tank is derived from the following equation

$$t = \frac{A_{\text{Tank}}}{A_{\text{Inlet,I}}} \sqrt{2\frac{h_{\text{I,Depth}}}{g}} \tag{8}$$

Thereby, it can be said that the entire immersion process takes 3 s.

Water-Release System Forest fires can behave differently depending on fuel type, humidity, wind strength and slope [67]. For light forest fires it is enough to moisten the fuel with 2 L m^{-2} to suppress fire for 20 min and for bigger fires 5 L m^{-2} are enough. However, some sources assume 0.10 L s^{-1} m^{-2} to extinguish severe forest fires [68][69]. Therefore, a one-size-fits-all solution is impractical because either water would be wasted, or not enough water would be used. This calls for a variable water-release system which can deploy enough water.
The flow rate $\dot{V}$ is depending on multiple variables such as the in tank water height h_{w}, which influences maximum outflow speed $v_{\text{o,max}}$, and outlet area A_{Outlet}. As the outflow takes place without additional pressurization, the Toricelli eq. (9) can be used, which calculates the time of the entire outflow process. The time to empty the tank is described by t_{o}. This allows the average outflow speed to be determined which influences the mass flow rate. Then, the amount of water reaching the fire $\dot{A}_{\text{e}}$ can be calculated, as shown in eq. (12). A conservative loss factor of 0.7, due to misting, is suggested [67].

$$t_{\text{o}} = \frac{A_{\text{Tank}}}{A_{\text{outlet}}} \sqrt{\frac{2h_{\text{w}}}{g}} \tag{9}$$

$$v_{\text{o,max}} = \sqrt{2gh_{\text{w}}} \tag{10}$$

$$\bar{v_{\text{o}}} = \frac{1}{t_{\text{o}}} \int_0^{t_{\text{o}}} v_{\text{o,max}} dt \tag{11}$$

$$\dot{A}_{\text{e}} = \frac{A_{\text{outlet}} \cdot \bar{v_{\text{o}}} \cdot \rho_{\text{water}} \cdot 0.7}{v_{\text{Flight}}} \tag{12}$$

Based on the previously shown equations (cf. eq. (9) to eq. (12)) and considering the required volumes of water, an outflow area of 0.05 to 0.15 m^2 must be used to provide the necessary flow rates.

4.7 Structure and Loads

In the following section, the structural concept of the INFERNO and its modules is presented. Moreover, the chapter describes the concept of the water tank and the allocated refilling and dumping mechanisms on a structural level.

4.7.1 Structural Concept of the Aircraft

Figure 4.14: Structural concept of fuselage with module installed

The structural concept of the INFERNO aircraft is characterized by the ability to withstand high loads during firefighting and scooping maneuvers while also considering a lightweight construction for a minimum **O**perating **E**mpty **W**eight (OEW). The primary structure consists of stringers and frames with two reinforced frames for the connection with the modular section. The density of stringers is higher in the upper and lower part of the fuselage as these parts of the aircraft encounter higher forces e.g. through the wing mounting or the landing gear integration. Furthermore, a higher density of frames in the tail area for the tailplane connection is considered. As shown in fig. 4.14, the complete structural integrity is only possible with the module installed. Fig. 4.15 depicts the fuselage wing structural concept of the wing. The wing structure consists of spars and ribs as well as pylons for the VTOL propeller integration. The front spear should be positioned at between 15 % and 30 % of the wing depth while the rear spear should be located at 67 % to 72 % in accordance with the positioning of the ailerons, the morphing wing actuators and the battery integration in the central wing box [31]. For additional stability, ribs were used for each wing in a span-wise direction. As the fuel tank is located inside the wing, the ribs have to guarantee the fuel flown inside the integral tank. The battery integration concept is shown in fig. 4.16. The tailplane mounting concept can be seen in figure . As depicted, the tail section is featuring a higher density of frames in order to realize enough stability for the mounting of the vertical tail and for the rudder forces which have to be transferred to the fuselage.

Figure 4.15: Structural concept of wing

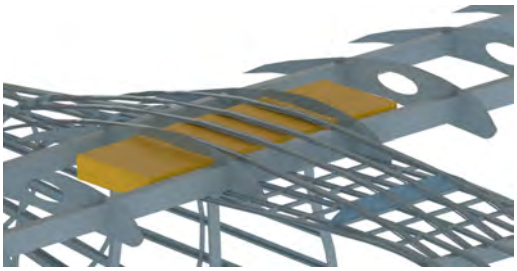

Figure 4.16: Structural concept of wing and battery integration

4.7.2 Structural concept of the modules

The modular part takes up a large part of the fuselage and cross-section, thus its capability to transfer loads during flight is essential for a safe operation. A structure of stringers and frames ensures compliance with the load transfer requirements. In the front and aft section of the module where the connection to the fuselage is made during assembly, the frames are reinforced and also feature specifically designed areas for the bolting connections. In the lower area of the module, the stringers are also reinforced as this section has to withstand high bending moments and longitudinal forces.

4.7.3 v-n Diagram

The v-n-diagram describes the aircraft limit load factors as a function of the flight speed. The limit load factors are defined as multiple of the standard gravity constant. Usually the highest loads that occur on an aircraft are generated by the lift during high-gravity maneuvers [29]. For lower flight speeds, the maximum load factor is limited by the maximum lift available, while at higher flight speeds it is limited by an arbitrary value that was chosen in the design of the aircraft [29]. Fig. 4.18 shows the calculated v-n diagram. A detailed calculation can be found in chap. A.12

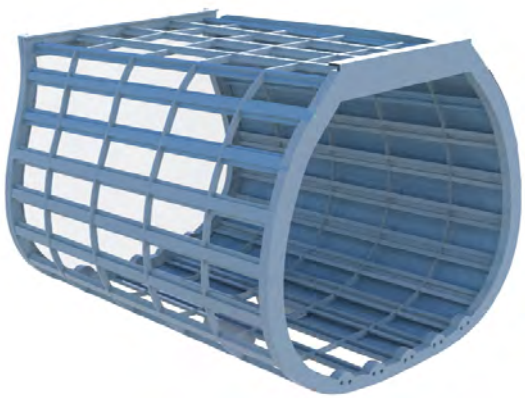

Figure 4.17: Structural concept of the modules

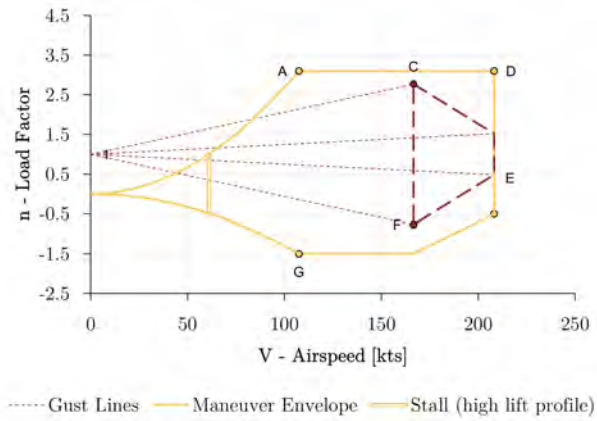

Figure 4.18: v-n diagram

4.8 Concept of Water Tank

The water tank is designed as an integral tank within the modular concept of the INFERNO in order to maximize the amount of water that can be carried with the module. As shown in fig. 4.19 which depicts the sectional view of the symmetrical tank, which is divided into three main sections with two separations in between. Thus, swapping water during maneuvering can be prevented. Moreover, the concept features two opening in the upper forward section for water filling on ground and to balance the pressure during refilling. As described in chap. 4.6, the INFERNO aircraft provides two mechanisms for refilling water during the mission. The scooping maneuver is using the two scooping inlets, water dropping and water refilling during hoovering is fulfilled by the water bay doors. The two water bay doors each feature two independently operable valves, which enables precise dropping maneuvers for different missions.

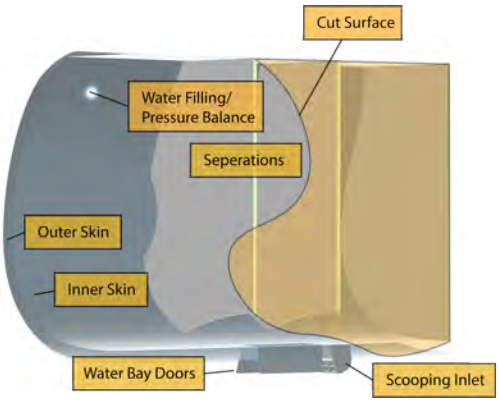

Figure 4.19: Concept of water tank

4.9 Noise Reduction

There are several ways to reduce noise in an aircraft. These options for noise reduction can be roughly divided into caused by the engine or the fuselage. However, it is not possible to influence the noise of the engine, as this is purchased directly from the manufacturer on the market, so no adjustments and optimizations are possible here. The noise of the airframe, on the other hand, can be divided into 3 categories. These are the wing including the tail surfaces and the fuselage, the high-lift devices and the landing gear [70].
The targeted optimum is the clean configuration. Since the morphing wing completely eliminates high-lift devices, maximum noise reduction is achieved in this section. For the landing gear, there are concepts with optimized fairings to avoid hard edges in the air flow. However, as this leads to an increase in weight, and the landing gear is only used when landing at the airport, but not when taking up water in lakes, this measure was dispensed with.

4.10 Minimising Hazards and Failures

During the design of INFERNO, diminished hazards and failures that endanger the safe operation of the aircraft was a key priority. Operating safely even in exceptional situations is essential for an effective firefighting operation. Both the vertical and horizontal electric motors are redundant so that controllability is still ensured in the event of a failure. In case of an engine failure, a restart or emergency landing can be initiated by the energy contained in the buffer battery. In the event of battery failure, it is possible to continue flying with reduced power provided by the turbine on a permanent basis. Due to the configuration similar to a fixed-wing aircraft, an emergency glider landing can still be initiated in the event of a complete failure of the propulsion unit. Due to this redundancy concept, no APU is necessary. As the water can be dropped in case of an emergency, critical flight phases with high payload can be avoided in an emergency. During the design process, a strong focus was put on the reduction of mechanically moving parts. By keeping moving equipment to a minimum, like through the elimination of propellers that can be moved in flight and the elimination of a flap system, manufacturing and maintenance costs and the probability of failure can be reduced. Moreover, the advanced cockpit systems ameliorates the safety standard of the INFERNO by assisting the pilot in various weather conditions and mission phases.

4.11 Configuration Summary

Fig. 4.20 depicts the payload-range diagram. The fuel ratios for engine start and warm-up, taxi, take-off, climb and landing were taken from Roskam [11] but were reduced in accordance with chap. 4.2.1 due to the lower cruise altitude and operation at small airports, that usually don't require a long taxi period. For CS-23 aircraft, there are no general regulations for additional safety fuel [71]. However, to operate the aircraft as safely as possible, extra fuel for an additional climb and for a 70 km flight to alternate airport, descent and landing were added. The value of 70 km was chosen. According to [72], for 95% of airports in Europe and 99% of airports in the United States of America an alternate airport for INFERNO can be found within 70 km. For missions where alternative airports are located further away, more safety fuel should be reserved. However, due to the VTOL capabilities, the aircraft can be landed safely even at provisional bases.

The maximum payload is 3000 kg and the range with this payload is 560 km. The standard mission payload is

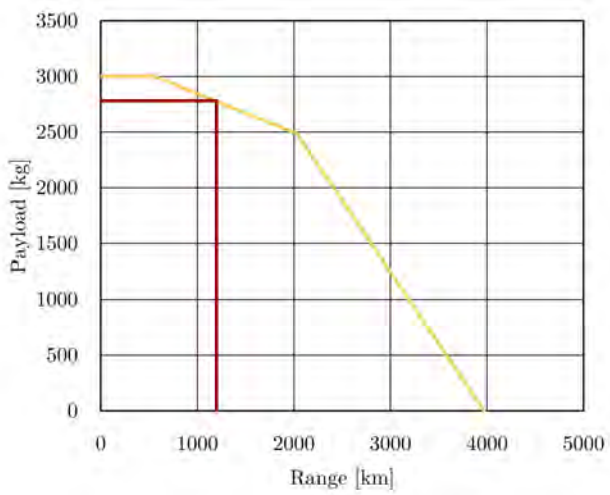

Figure 4.20: Payload-Range diagram

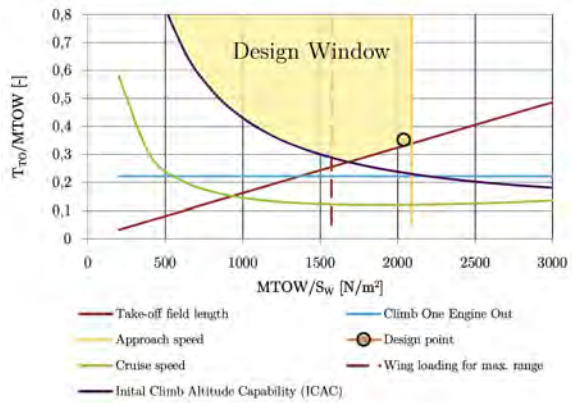

Figure 4.21: Sizing diagram

2800 kg per aircraft, which leads to a design range of 1200 km, as calculated in chap. 2.1. The ferry range is 4000 km, which enables INFERNO to flexible proceed within Europe and Northern Africa without limitations.

5 Fleet Concept

In the following chapter, the unique fleet concept of the INFERNO aircraft is described, including the flexible modular design as well as its operational concept.

5.1 Modularity

Due to its modular structure, INFERNO is able to fulfill a wide range of tasks. Customers will be able to choose between three modules when it goes into service in 2030. More modules could be offered at a later date. In addition to the firefighting module, there will also be a cargo version and a passenger version. The cargo version with a maximum load of 3000 kg has two swiveling side doors, which ensures easy loading, even with large items (cf. fig. 5.1). The cargo can be secured through eyelets of the flat cargo floor. The passenger version has 5 seats arranged opposite each other (cf. fig. 5.2). The cross-section is designed so that all seats have a minimum seat height of 0.95 m. Behind the second row of seats, there is space for smaller pieces of luggage. Boarding and de-boarding is done via a door on the left side of the module. It opens in a way ensuring that passengers are protected by the door from the propeller. This is especially important in case of emergency evacuation.
In the following, a few explanations about the installation of the exchange module will be given. To avoid unnecessary stress on the structure in the upper section during the assembly process, no payload should be on board for the replacement and the fuel should be drained. The replacement process is carried out in four steps. In the first step, the left propeller is folded up. To reduce the maintenance effort and complexity, the folding mechanism is only possible in the ground position. Subsequently, a tail support must be attached, since the COG position cannot be covered by the landing gear without the module. Now the desired module can be transported to the aircraft with the help of special forks. The special forks are forks that are adapted to the shape of the module. The module is then transported as close to the ground as possible to the aircraft and positioned in the X direction. In the third step, the module is then retracted into the fuselage in the Y direction and raised in the Z direction. In this position, the module can be inserted into the guide rollers provided. To be able to retract the module quickly and without damage, the right outer shell is smaller than the left one. The guide rollers are conical, which means that the module is automatically centered in the X and Z directions when it is retracted. When the module is fully retracted, it is bolted to the stringer flange. In this way, the module can also transmit forces in the longitudinal direction. The bolting mechanism is designed with the help of a cardan shaft so that it can be fixed from the outside. The tail support can then be removed again. Finally, the propeller can be folded down again. A visualization of the assembly process can be found in app. A.3. The module is disassembled in reverse order.

The modular approach not only offers the operator a very high degree of flexibility, but can also ensure high utilization of the aircraft throughout the year thanks to the rapid replacement process (cf. chap. 5.2). Furthermore, all versions can be produced on one production line. Only the production of the modules has to be differentiated. This means that modularity is also characterized by low costs (cf. chap. 6).

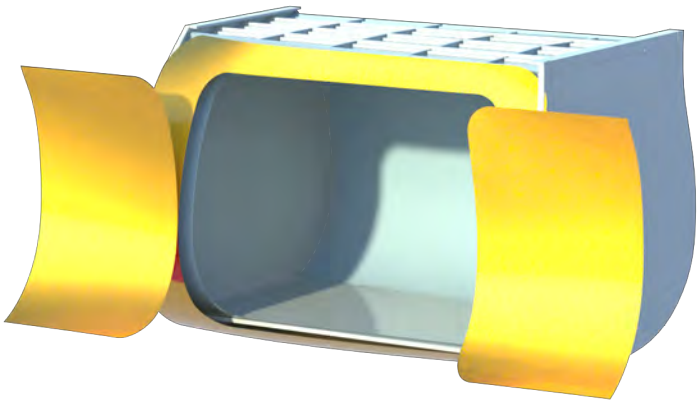

Figure 5.1: Cargo version

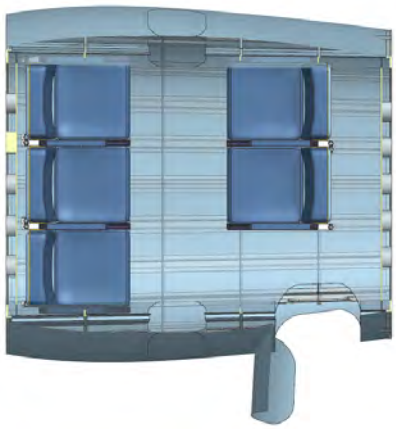

Figure 5.2: Passenger version

5.2 Operational Concept

This section provides an overview of the operational concept on a daily and yearly basis and presents further operational aspects that characterize the INFERNO aircraft.

5.2.1 Operational Concept 24-Hour Mission

The operational concept of the INFERNO firefighting mission is intended to optimize the dropped amount of water during a 24 h mission. For the intended mission, four firefighting aircraft are needed in order to achieve the necessary amount of dropped water within one approach of the fleet. For a successful 24 h operation, a total of 10 flight crews are necessary in order to guarantee enough rest times and work hour limits for the crews. At the beginning of each mission, the INFERNO aircraft are ferried to the operational base for the intended firefighting mission. They are accompanied by one INFERNO aircraft equipped with the passenger module and one with the freight module. The PAX version is carrying five additional pilots for the mission, while the cargo version is carrying necessary equipment like water pumps, material for a field base for the mission planning and crew preparation, spare parts and tools. Furthermore, the PAX version has to carry one additional pilot, who is positioned on a jump seat within the module. After reaching the operational base for the mission, the four firefighting aircraft named Poseidon, Taru, Fons and Aegir are prepared for the operation with the water tank being filled, the aircraft being refueled and the pilots preparing the aircraft for take-off. The additional PAX and freight version are ferried to the next mission or can be used for aerial refilling and observation or as back-up aircraft in the case of technical issues. For the first mission, four crews which could rest during the ferry flight with the PAX version are planned to be in control. As the INFERNO concept features an optional aerial refueling capability, the two scenarios have to be considered separately. Figure 5.3 shows the operational concept, including the refueling in flight. As shown, the flight time of several flights can be doubled and returns to the base can be minimized. By using this concept, six proceedings to and from the operational base can be avoided, which equals an additional flight time within the mission area of 6 h. Nevertheless, the aerial refueling feature is not suitable for every mission, thus the operational concept with the classical INFERNO configuration is considered in figure 5.4.

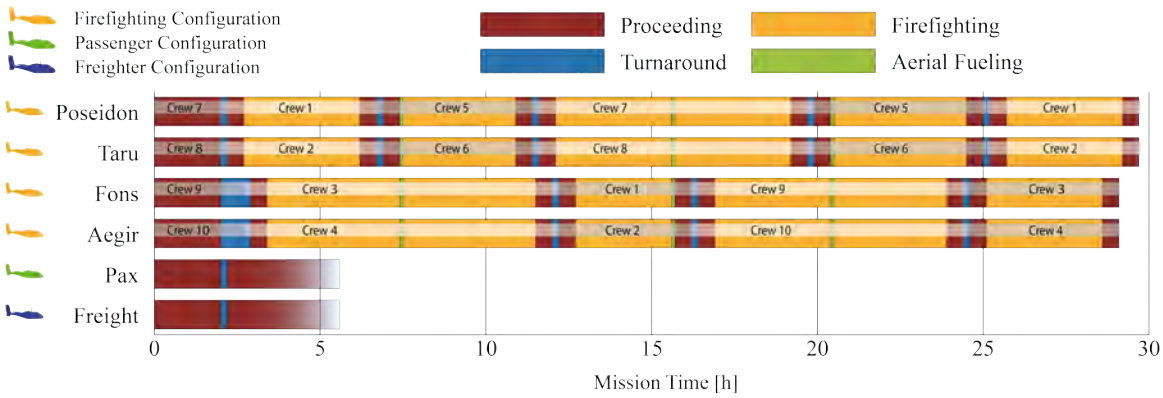

Figure 5.3: Fleet concept of the INFERNO aircraft using the aerial refueling capability

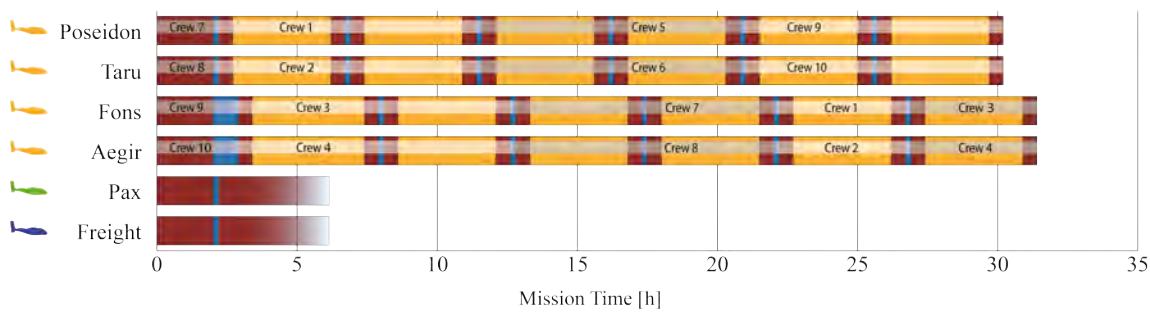

Figure 5.4: Fleet concept of the INFERNO aircraft without aerial refueling

5.2.2 Annual Operational Concept

An annual operation scheme for the INFERNO mission is a subject matter to the wildfire seasons, which can be analysed by studying the yearly number of wildfires and the respective amount of burned area around the globe. For the preliminary concept design discussed within this section, Europe was chosen as the area of operational interest. Wildfire trends and cumulative burned area per month across the span of the past 15

years (2006 to 2021) were made available by the European Forest Fire Information System (EFFIS) of the EU Copernicus program [73], [74]. This data was then statistically analysed for determining the annual wildfire seasons in the European continent and the total surface area affected on a monthly and daily basis. A quick tabular overview of the average number of wildfires and average burned area per month over the past two decades effectively revealed the months of a year with low, moderate, and peak wildfire activity of Europe and the United States (cf. app. A.6, tab. A.1, A.2, and A.3 respectively). Wildfires in grasslands and forests spread rapidly, and it could be hours or even days before one is recognized. It is to be realized that the EFFIS provides numbers for the total area burned from the wildfires after they are extinguished. For the INFERNO operational concept, as there is no certainty when the exponentially growing wildfire would be recognized, a 70% value of the total burned area value was assumed as the alarm point for when the authorities recognize the wildfire and respond to it. The tactic would be to spray down the extinguishing agent i.e., in the current design water, across a 20 m circumference width around the wildfire to stop it from propagating forward. With additional intermediate steps, an average area to be sprayed per day was calculated to estimate the average count of INFERNOs required per day per month of the year to fight the fire. An additional INFERNO is also assigned to the firefighting batch with rescue and cargo modularity in the form of extended humanitarian aid for the distressed victims of the wildfire.

For Europe (**E**uropean **U**nion (EU) + Non-EU), a maximum of eight INFERNOs or 32 aircraft are required for the yearly operational concept. This means that a fleet of eight of each Aegir, Fons, Poseidon, and Taru aircraft shall be deployed for a yearlong firefighting operation across the continent. As mentioned above, not all months experience equally vigorous wildfires and so during the season of comparatively lesser wildfires, a considerable number of Poseidon, and Fons and Taru are assigned fleet duty as cargo and passenger (Pax) aircraft respectively.

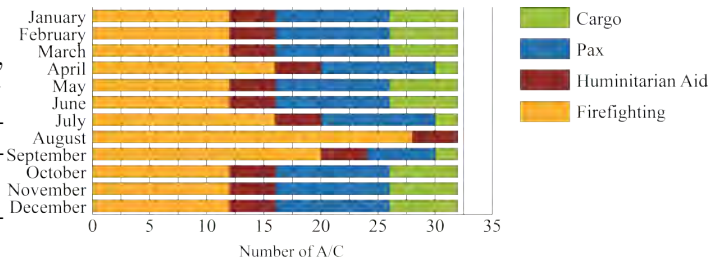

Figure 5.5: Yearly Fleet concept of the INFERNO aircraft

Aegir is sustained for a yearlong firefighting duty and is accompanied continuously in operation with its other fleet members depending on the mission definition and wildfire severity. A vivid graphical representation of the yearly operation concept comprising the annual fleet management concept is realized in Fig. 5.5. The cumulative annual operation time of INFERNO operating in Europe is 6552.6 h, which results in a total operation downtime of 2207.4 h, see tab. A.7. For the **U**nited **S**tates of **A**merica (USA), currently only the annual firefighting operation concept (cf. tab. A.8) is prepared with a total yearly firefighting time of 8073 h. A operation concept for the USA defining annual Pax and cargo duties for INFERNO fleet could also be developed similarly, as done for Europe.

5.2.3 Formation Flight

To increase the efficiency of the fleet on longer routes and to reduce emissions, formation flight is used. Savings of up to 18 % for the following aircraft have already been demonstrated in flight tests [75], [76]. However, flight controllers available today for automated formation flight are only stable outside the wake vortex inflow area [77]. For this reason, formation flight should be carried out within the centre field. This corresponds to a distance of 15 to 150 wingspan of the aircraft. This area also has the advantage that the aircraft structure is significantly less stressed. However, the savings potential here is only up to 10 % [78], [79]. The exact sweep spot is to be found during the further development process with the help of a suitable simulation method.

5.2.4 Aerial Refueling

INFERNO has a very large wing and can therefore store more fuel chap. 4.2.6, than required for the optimal 1200 km range, that was specified for the design mission in chap. 2.1. If, for example, the operational base for refueling is further away than in the design mission and there should be no payload limitations. The flight to and from the operational basis are very time-consuming and limit the dropped amount of water within a 24 h time slot. Due to its additional fuel tank capacity of 330 l an optional aerial

Figure 5.6: Drogue-and-probe concept for aerial refueling and maximizing firefighting time

refueling mechanism can be installed. With aerial refueling, only one out of the two aircraft have to return to the base and thus the time at the fire can be increased by 80% without payload limitations. After the fuel that was obtained by refueling is consumed, the second aircraft return to the base to fuel up and change the pilot. Fig. 5.6 shows the additional equipment that is installed on the aircraft, that are equipped with the aerial refueling mechanism.

5.2.5 Turnaround and Ground Handling

The ground handling process of the INFERNO aircraft is dominantly influenced by the refueling and water refilling process. As depicted in fig. 5.7, those activities can be processed simultaneous. Fig. 5.8 displays the calculated times for the overall turnaround at the operational base also considering the **G**round **S**upport **E**quipment (GSE) positioning and the flight preparations by the pilot. With considering a pump performance of 470 L min^{-1}, the water tank can be refilled within six min. while the refueling is calculated with five min. The critical path for the overall turnaround is the water refilling. The whole process can be realized within a 16 min time frame.

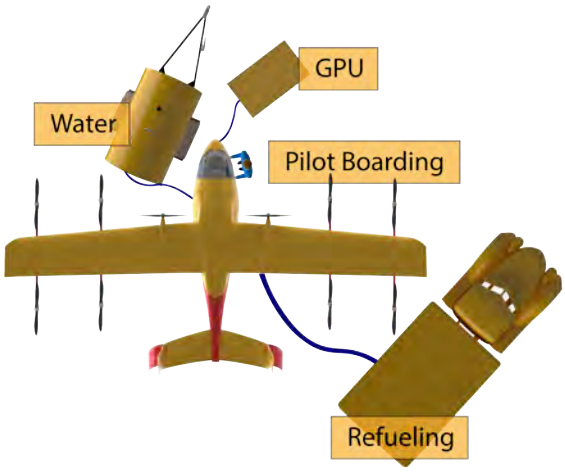

Figure 5.7: Turnaround drawing

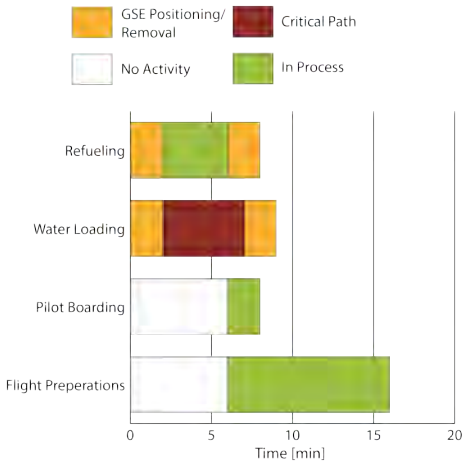

Figure 5.8: Turnaround time chart

6 Cost Analysis

This section of the report provides a detailed overview of the cost analysis for the novel INFERNO concept. Two main aircraft cost parameters discussed in this section are the **L**ife **C**ycle **C**ost (LCC) and the **D**irect **O**perating **C**osts (DOC). During calculations, the parameters had been adapted to diverse unitary systems, but the representation of the LCC and DOC throughout this section is uniformly illustrated in Euros [€].

6.1 Life Cycle Cost

The LCC, as the self-explanatory term goes, is the cost comprising the variable and predictable finances required for the aircraft from its idea's genesis till the end of its operational life. The preliminary LCC estimation for the INFERNO concept has an estimable impact on the total fleet program cost, which depends highly on the initial design costs. The total LCC is a sum of the individual cost estimations allocated to the 'Development, Test and Acceptance/Certification' and the 'Production'. The formulas employed for LCC calculation are adapted from Nicolai– Fundamentals of Aircraft & Airship Design [80] and represent the costs in 1998 US-$. Additionally, necessary INFERNO design parameters were initially converted into required units from their respective metric system values before plugging them into the cost calculation formulas. The calculated costs are then multiplied with the 1998 Dollar to Euro conversion rate and overall dollar inflation factor of 1.4787 obtained for a timeline of 1998 to 2030.
The 'Development, Test and Acceptance/Certification' costs sum up to a total of 102.97 million €. Cumulative 'Production' cost incorporates the tolling costs, cost for **Q**uality **A**ssurance (QA), powertrain costs, **B**ill of **M**aterial (BOM), and aircraft production costs. It depends on the total number of aircraft produced and for a foreseen production of 700 aircraft, the total 'Production' cost calculated is 666.04 million €. Consequently, the total LCC cost for the INFERNO program is estimated at 769 million €. This substantially translates to a per

aircraft LCC of 1.46 million €, which also incorporates an expenditure of 200,000 € per aircraft for the glass cockpit and IFR, and an **E**xpenditure **B**efore **I**nterest and **T**axes (EBIT) margin of 15%. Tab. A.9 provides a categorically simplified structure to the LCC calculations of the INFERNO program.

6.2 Direct Operation Cost

The framework employed to deduce the DOC for the INFERNO aircraft concept is of the Thorbeck method by J. Thorbeck from the Technical University of Berlin [81]. The DOC is a direct sum of the following five main costs i.e., the fuel costs; navigation, landing, and ground handling fees; maintenance costs; crew costs; and capital costs relating to hedge and insurance. A graphical representation of the distribution of these costs on a percentage basis is illustrated in fig. 6.1. The formulas, used for calculating the DOC from [34] adapted from the works of J. Thorbeck [81], return the cost results in 2010-€. All costs are calculated with a presumed operation kick-off in 2030 and are, therefore, adjusted using the presumed rate of inflation from 2010 to 2030. By these means, after the calculation of the five DOC building costs, the absolute DOC for the INFERNO program is calculated at 3.7 million €/year. The absolute DOC per year is further translated into 3501 €/FC, 292 €/100 km, and 58 €/100 km/Pax. The unit €/FC represents the cost per flight cycle (1200 km flight), €/100 km represents the costs per 100 flight kilometres, and €/100 km/Pax the costs per 100 flight kilometres per passenger. Tab. A.10 provides an overview of the necessary factors and quantities, along with the total DOC for the INFERNO program.

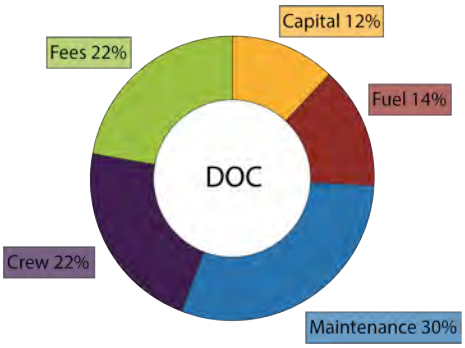

Figure 6.1: Percentage distribution of the five DOC building costs

7 Evaluation

7.1 Fulfillment of the Design Specifications

REQ-ID	INFERNO	Achievement
#1	VTOL and STOL capabilities	achieved
#2	11 000 l within one approach	achieved
#3	Modular Design and high yearly utilization	achieved
#4	EIS 2030	achieved
#5	Minimizing risks during operation	achieved
#6	Minimizing noise and emissions	achieved
#7	MTOM below 5670 kg	achieved
#8	Smooth transition between flight phases	to be confirmed with CFD simulation

Table 7.1: Overview of the achieved requirements

7.2 Conclusion

Fighting wildfires is one of the major challenges rapidly gaining significance with global warming on the rise. The INFERNO aerial firefighting concept developed as a result of the 2022 DLR Design Challenge presents a state-of-the-art aircraft designed to efficiently respond to wildfire scenarios around the globe. The concept features profound technologies to guarantee the best possible flight characteristics for these demanding missions. Thus, the INFERNO concept combines the flexibility of a VTOL aircraft with a conventional fixed wing concept for efficiency during cruise. Thereby, both water refilling during hovering and scooping during the forward flight can be achieved leading to broad possibilities during various wildfire missions. The INFERNO aircraft is equipped with a serial hybrid system featuring a fuel efficient engine, a modern generator and a state-of-the-art battery concept supplying 10 electrically driven propeller, eight for the VTOL capabilities and two for the propulsion during forward flight. Moreover, the design is equipped with a modular fuselage part which can be flexible changed between the water tank, a passenger or a cargo module. Thus, an efficient year round fleet concept was developed minimizing ground times and operating costs. Additionally, a specific concept for the INFERNO firefighting missions was designed optimizing the amount of water carried and dropped during the operation. Therefore, a fleet of four firefighting versions is needed.

Bibliography

[1] P. Hirschberger, "WÄLDER IN FLAMMEN - Ursachen und Folgen der weltweiten Waldbrände," 2012.

[2] Umweltbundesamt, *Waldbrände*, 6.07.2022. [Online]. Available: https://www.umweltbundesamt.de/daten/land-forstwirtschaft/waldbraende#waldbrande-in-deutschland (visited on 07/06/2022).

[3] Deutsches Zentrum für Luft- und Raumfahrt, "DLR Design Challenge 2022," 2022. [Online]. Available: https://www.dlr.de/content/en/downloads/2022/dlr-design-challenge-2022-task-v1-4.pdf;jsessionid=1E9F991938632DEABC9C0D06235AD568.delivery-replication1?__blob=publicationFile&v=4 (visited on 07/06/2022).

[4] Zki, *DLR - Earth Observation Center - MODIS Fire Service*, Jul. 2, 2022. [Online]. Available: https://www.dlr.de/eoc/en/desktopdefault.aspx/tabid-12938/22428_read-51632/ (visited on 07/02/2022).

[5] Brandon Maccherone, *Modis web*, Jul. 2, 2022. [Online]. Available: https://modis.gsfc.nasa.gov/data/dataprod/mod14.php (visited on 07/02/2022).

[6] VIKING, *Performance and Operating Data CL-415*, Viking, Ed., 2020. [Online]. Available: https://aerialfirefighter.vikingair.com/firefighting/performance-operating-data (visited on 06/30/2022).

[7] J. C. [Publishers], Ed., *Jane's all the world's aircraft*, Englisch, Zeitschrift, Coulsdon, Surrey, 2020.

[8] D. Finger, "Vergleichende Leistungs- und Nutzenbewertung von VTOL- und CTOL-UAVs," *Luft- und Raumfahrt*, vol. 2017, pp. 44–47, Jan. 2017.

[9] A. Bacchini and E. Cestino, "Electric VTOL Configurations Comparison," *Aerospace*, vol. 6, no. 3, 2019, ISSN: 2226-4310. DOI: 10.3390/aerospace6030026. [Online]. Available: https://www.mdpi.com/2226-4310/6/3/26.

[10] L. Gaines, J. Sullivan, A. Burnham, and I. Belharouak, "Life-cycle analysis of production and recycling of lithium ion batteries," *Transportation Research Record*, vol. 2252, no. 1, pp. 57–65, 2011. DOI: 10.3141/2252-08. eprint: https://doi.org/10.3141/2252-08. [Online]. Available: https://doi.org/10.3141/2252-08.

[11] D. J. Roskam, *Airplane Design Part III: Layout of Cockpit, Fuselage, Wing and Empennage: Cutaways and Inboard Profiles*. Darcoperation, 2017, ISBN: 188488556X.

[12] D. Z. für Luft-und Raumfahrt, *100 Prozent nachhaltiger Kraftstoff zeigt Perspektive für Passagierflugzeuge*, 6.07.2022. [Online]. Available: https://www.dlr.de/content/de/artikel/news/2021/04/20211129_100-prozent-saf-kraftstoff-zeigt-perspektive-fuer-passagierflugzeuge.html (visited on 07/06/2022).

[13] M. Greenwood, J. M. Wrogemann, R. Schmuch, H. Jang, M. Winter, and J. Leker, "The battery component readiness level (bc-rl) framework: A technology-specific development framework," *Journal of Power Sources Advances*, vol. 14, p. 100 089, 2022, ISSN: 2666-2485. DOI: https://doi.org/10.1016/j.powera.2022.100089. [Online]. Available: https://www.sciencedirect.com/science/article/pii/S2666248522000075.

[14] Seitz, Arne and Habermann, Anaïs Luisa and Peter, Fabian and Troeltsch, Florian and Castillo Pardo, Alejandro and Della Corte, Biagio and van Sluis, Martijn and Goraj, Zdobyslaw and Kowalski, Mariusz and Zhao, Xin and Grönstedt, Tomas and Bijewitz, Julian and Wortmann, Guido, "Proof of concept study for fuselage boundary layer ingesting propulsion," *Aerospace*, vol. 8, no. 1, 2021, ISSN: 2226-4310. DOI: 10.3390/aerospace8010016. [Online]. Available: https://www.mdpi.com/2226-4310/8/1/16.

[15] M. Rendon, C. Sanchez, J. Gallo, and A. Anzai, "Aircraft hybrid-electric propulsion: Development trends, challenges and opportunities," *Sba Controle & Automacao Sociedade Brasileira de Automatica*, Jun. 2021. DOI: 10.1007/s40313-021-00740-x.

[16] D. Li, S. Zhao, A. Da Ronch, *et al.*, "A review of modelling and analysis of morphing wings," *Progress in Aerospace Sciences*, vol. 100, pp. 46–62, 2018, ISSN: 0376-0421. DOI: https://doi.org/10.1016/j.paerosci.2018.06.002. [Online]. Available: https://www.sciencedirect.com/science/article/pii/S0376042117301835.

[17] MTU AEROREPORT, *Modulare Flugzeuge: Flexibilität soll Kosten sparen*. [Online]. Available: https://aeroreport.de/de/innovation/modulare-flugzeuge-flexibilitaet-soll-kosten-sparen (visited on 07/06/2022).

[18] W. Electric, *Electric motor*. [Online]. Available: https://www.weflywright.com/technology#motors (visited on 07/05/2022).

[19] *LiDAR Scanners and Sensor Applications at RIEGL USA*. [Online]. Available: {https://www.rieglusa.com/lidar-scanners-and-sensors-applications.html} (visited on 07/11/2022).

[20] *Flightcell DZMx*, 2020. [Online]. Available: {https://www.flightcell.com/products/flightcell-dzmx} (visited on 07/11/2022).

[21] Prof. Dipl.-Ing. R. Voit-Nitschmann, "Einführung in die Luftfahrttechnik: Begleitmaterial zur Vorlesung: Version 5.2," Version 5.2, Stuttgart, April 2011.

[22] Prof. Dipl.-Ing. Voit-Nitschmann, "Flugzeugentwurf II," Stuttgart, April 2006.

[23] L. Carrino, "Foreword 2," in *Morphing Wing Technologies*, A. Concilio, I. Dimino, L. Lecce, and R. Pecora, Eds., Butterworth-Heinemann, 2018, pp. li–lii, ISBN: 978-0-08-100964-2. DOI: https://doi.org/10.1016/B978-0-08-100964-2.09982-2. [Online]. Available: https://www.sciencedirect.com/science/article/pii/B9780081009642099822.

[24] D. Coutu, V. Brailovski, and P. Terriault, "Optimized design of an active extrados structure for an experimental morphing laminar wing," *Aerospace Science and Technology*, vol. 14, no. 7, pp. 451–458, 2010.

[25] B. K. Woods, J. H. Fincham, and M. I. Friswell, "Aerodynamic modelling of the fish bone active camber morphing concept," in *Proceedings of the RAeS Applied Aerodynamics Conference, Bristol, UK*, vol. 2224, 2014.

[26] M. M. S. Reza, S. A. Mahmood, and A. Iqbal, "Performance analysis and comparison of high lift airfoil for low speed unmanned aerial vehicle," International Conference on Mechanical Industrial & Energy Engineering, 2016.

[27] P. D. R. Eppler, *Airfoil Design and Data*. Springer-Verlag Berlin Heidelberg, 1990, ISBN: 978-3-662-02648-9.

[28] Prof. Dr. -Ing. Thorsten Lutz, *Flugzeugaerodynamik I & II*.

[29] D. P. Raymer, *Aircraft design: A conceptual approach*, Sixth edition, ser. AIAA education series. Reston, Virginia: American Institute of Aeronautics and Astronautics, Inc., 2018, ISBN: 978-1-62410-490-9.

[30] E. Torenbeek, *Advanced Aircraft Design: Conceptual Design, Analysis and Optimization of Subsonic Civil Airplanes*. John Wiley & Sons, 2013, ISBN: 978-1-118-56811-8.

[31] PROF. DR.-ING. DIETER SCHOLZ, *Skript zur Vorlesung Flugzeugentwurf*, 1999.

[32] Prof. Dr.-Ing. Andreas Strohmayer, *Flugzeugentwurf I*.

[33] I. Buchweitz, *Flugzeugentwurf am Beispiel eines ausgeführten Flugzeugs*, Hochschule für Angewandte Wissenschaften Hamburg, Fachbereich Fahrzeugtechnik, Ed., Hamburg, Feb. 15, 2002.

[34] Prof. Dr.-Ing. Andreas Strohmayer, *Flugzeugentwurf II*.

[35] S. Gudmundsson, *General aviation aircraft design: Applied methods and procedures*, 1st ed. Oxford, UK: Butterworth-Heinemann, 2014, ISBN: 978-0-12-397308-5.

[36] B. G. van der Wall, *Grundlagen der Hubschrauber-Aerodynamik*, 1st ed., ser. VDI-Buch. Berlin, Germany: Springer-Verlag, 2015, ISBN: 978-3-662-44400-9. DOI: https://doi.org/10.1007/978-3-662-44400-9.

[37] Xiaolong Zhang, Cheryl L. Bowman, Tim C. O'Connell, and Kiruba S. Haran, "Preliminary design of the superconducting rotor for nasa's high-efficiency megawatt motor," *IET Electric Power Applications*, 2017.

[38] J. J. Dr. Scheidler, "Large electric machines for aircraft electric propulsion," NASA, 2018.

[39] G. E. Aviation, *Future of flight*, G. Aviation, Ed. [Online]. Available: https://www.geaviation.com/future-of-flight (visited on 07/05/2022).

[40] ——, *H-Series Turboprop engine family — Engines on a mission*, G. Aviation, Ed. [Online]. Available: https://www.geaviation.com/propulsion/regional-business/h-series (visited on 07/05/2022).

[41] Peter deBock, *GE Turbines and small Engines Overview*, General Electric, Ed., 2019. [Online]. Available: https://arpa-e.energy.gov/sites/default/files/14_deBock_GETurbinesandsmallenginesoverview-ARPA-eINTEGRATEV2.pdf#page=8 (visited on 07/11/2022).

[42] P. Z. S. Spakovszky, "Implications of propulsive efficiency for engine design," D. Quattrochi, Ed., [Online]. Available: http://web.mit.edu/16.unified/www/FALL/thermodynamics/notes/node82.html (visited on 07/05/2022).

[43] European Union Aviation Safety Agency, *TYPE-CERTIFICATE DATA SHEET No.E.070 for M601/H80 series engines*, EASA, Ed. [Online]. Available: https://www.easa.europa.eu/downloads/7685/en (visited on 07/05/2022).

[44] ——, *TYPE-CERTIFICATE DATA SHEET No. P.104 for MTV-27 series propellers*, EASA, Ed. [Online]. Available: https://www.mt-propeller.com/pdf/TCDS_EASA/MTV-27.pdf (visited on 07/05/2022).

[45] ——, *TYPE-CERTIFICATE DATA SHEET No. EASA.P.100 for MTV-20 series propellers*, EASA, Ed. [Online]. Available: https://www.mt-propeller.com/pdf/TCDS_EASA/MTV-20.pdf (visited on 07/05/2022).

[46] YASA, *Yasa-750r electric motor product sheet.* [Online]. Available: https://www.yasa.com/wp-content/uploads/2021/05/YASA-750RDatasheet-Rev-11.pdf (visited on 07/06/2022).

[47] Mikhaylik, Y., Kovalev, I., Scordilis-Kelley, Y., Liao, L., Laramie, M., Schoop, U., and Kelley, T., *650 Wh/Kg, 1400 Wh/L Rechargeable Batteries for New Era of Electrified Mobility.* [Online]. Available: https://www.scribd.com/document/467075308/650-whkg-1400-whl-recharg-batt-new-era-elect-mobility-ymikhaylik-0-pdf (visited on 07/02/2022).

[48] SUAVE: An Aerospace Vehicle Environment for Designing Future Aircraft, *Sizing.* [Online]. Available: https://suave.stanford.edu/doxygen/group__Methods-Power-Battery-Sizing.html (visited on 07/05/2022).

[49] A. Misra, "Summary of 2017 NASA Workshop on Assessment of Advanced Battery Technologies for Aerospace Applications," in *AIAA SciTech Forum and Exposition*, 2018.

[50] S. N. Motapon, E. Lachance, L.-A. Dessaint, and K. Al-Haddad, "A generic cycle life model for lithium-ion batteries based on fatigue theory and equivalent cycle counting," *IEEE Open Journal of the Industrial Electronics Society*, vol. 1, pp. 207–217, 2020. DOI: 10.1109/OJIES.2020.3015396.

[51] T. Energies, *Sicherheitsdatenblatt gemäß Verordnung (EG) Nr. 1907/2006 JET A-1*, 2018. [Online]. Available: https://services.totalenergies.de/sites/g/files/wompnd2336/f/atoms/files/sicherheitsdatenblatt_jet_a1.pdf.

[52] CENTRELINE, *Centreline website.* [Online]. Available: https://www.centreline.eu/innovation/ (visited on 07/10/2022).

[53] A. Seitz, F. Peter, J. Bijewitz, A. Habermann, Z. Goraj, M. Kowalski, A. Pardo, C. Hall, F. Meller, R. Merkler, O. Petit, S. Samuelsson, B Corte, M. Sluis, G. Wortmann, M. Dietz, "Concept validation study for fuselage wake-filling propulsion," Bauhaus Luftfahrt e.V., Warsaw University of Technology, University of Cambridge, Airbus Innovations, MTU Aero Enignes, Chalmers University of Technology, Technical University of Delft, Siemens AG, ARTTIC, 2018.

[54] S. Metals, *Inconel alloy 625.* [Online]. Available: https://www.specialmetals.com/documents/technical-bulletins/inconel/inconel-alloy-625.pdf (visited on 07/11/2022).

[55] J. Benzaquen, J. He, and B. Mirafzal, "Toward more electric powertrains in aircraft: Technical challenges and advancements," *CES Transactions on Electrical Machines and Systems*, vol. 5, no. 3, pp. 177–193, 2021. DOI: 10.30941/CESTEMS.2021.00022.

[56] M. Hepperle, "Electric flight - potential and limitations," in *Energy Efficient Technologies and Concepts of Operation*, Oct. 2012. [Online]. Available: https://elib.dlr.de/78726/.

[57] *Primus epic block 3 upgrade for Gulfstream G650/G650ER.* [Online]. Available: {https://aerospace.honeywell.com/us/en/products-and-services/product/hardware-and-systems/cockpit-systems-and-displays/primus-epic-block-3-for-gulfstream-g650-g650er} (visited on 07/11/2022).

[58] *Primus Apex Integrated Flight Deck.* [Online]. Available: {https://aerospace.honeywell.com/us/en/products-and-services/product/hardware-and-systems/cockpit-systems-and-displays/primus-apex} (visited on 07/11/2022).

[59] *Multi-Function Radar Display (MFRD).* [Online]. Available: {https://aerospace.honeywell.com/us/en/products-and-services/product/hardware-and-systems/cockpit-systems-and-displays/multi-function-radar-display} (visited on 07/11/2022).

[60] *Head-up Display*, 2022. [Online]. Available: {https://en.wikipedia.org/wiki/Head-up_display} (visited on 07/11/2022).

[61] *Electronic Centralized Aircraft Monitor (ECAM)*, 2021. [Online]. Available: {https://skybrary.aero/articles/electronic-centralized-aircraft-monitor-ecam} (visited on 07/11/2022).

[62] W. Lijing, X. Wei, H. Xueli, *et al.*, "The virtual evaluation of the ergonomics layout in aircraft cockpit," in *2009 IEEE 10th International Conference on Computer-Aided Industrial Design & Conceptual Design*, IEEE, 2009, pp. 1438–1442.

[63] Yeh, Michelle and Swider, Cathy and Jo, Young Jin and Donovan, Colleen and others, "Human Factors Considerations in the Design and Evaluation of Flight Deck Displays and Controls," John A. Volpe National Transportation Systems Center (US), Tech. Rep., version 2.0, 2016.

[64] R. van der Pluijm, "Cockpit design and integration into the flying v," 2021.

[65] *Talon MMS*. [Online]. Available: {https://www.flir.com/products/talon-mms/} (visited on 07/11/2022).

[66] AgAir Update Staff, *CACI's Aerial Sensor Technology provides real-time heat mapping data and reduces risk to firefighters*, 2020. [Online]. Available: {https://aerialfiremag.com/2020/10/27/cacis-aerial-sensor-technology-provides-real-time-heat-mapping-data-and-reduces-risk-to-firefighters/} (visited on 07/11/2022).

[67] G. Penney, D. Habibi, M. Cattani, and M. Carter, "Calculation of critical water flow rates for wildfire suppression," *Fire*, vol. 2, no. 1, 2019, ISSN: 2571-6255. DOI: 10.3390/fire2010003. [Online]. Available: https://www.mdpi.com/2571-6255/2/1/3.

[68] R. Hansen, "Corrigendum to: Estimating the amount of water required to extinguish wildfires under different conditions and in various fuel types," *Wildland Fire*, vol. 21, p. 778, 2012. DOI: 10.1071/WF11022_CO.

[69] K. Satoh, I. Maeda, K. Kuwahara, and K Yang, "A numerical study of water dump in aerial fire fighting," *Fire Safety Science*, vol. 8, pp. 777–787, 2005.

[70] G. M. L. David P. Lockard, "The airframe noise reduction challenge," 2004.

[71] European Union Aviation Safety Agency, *Certification Specifications and Acceptable Means of Compliance for Normal, Utility, Aerobatic and Commuter Aeroplanes CS-23: CS-23*, 2020.

[72] I. Geiß and A. Strohmayer, *Operational Energy and Power Reserves for Hybrid-Electric and Electric Aircraft*. Deutsche Gesellschaft für Luft- und Raumfahrt - Lilienthal-Oberth e.V., 2021.

[73] D. Aifantopoulou *et al.*, "Copernicus emergency management service," *10442/15383*, pp. 00–54, 2016.

[74] *Welcome to EFFIS*. [Online]. Available: https://effis.jrc.ec.europa.eu/.

[75] M. J. Vachon, R. Ray, K. Walsh, and K. Ennix, "F/a-18 aircraft performance benefits measured during the autonomous formation flight project," in *AIAA Atmospheric Flight Mechanics Conference and Exhibit*, [Reston, Va.]: [American Institute of Aeronautics and Astronautics], 2002, ISBN: 978-1-62410-107-6. DOI: 10.2514/6.2002-4491.

[76] C. Hanson, J. Ryan, M. Allen, and S. Jacobson, "An overview of flight test results for a formation flight autopilot," in *AIAA Guidance, Navigation and Control Conference and Exhibit*, [Reston, Va.]: [American Institute of Aeronautics and Astronautics], 2002, ISBN: 978-1-62410-108-3. DOI: 10.2514/6.2002-4755.

[77] A. K. R. Luckner, "Formationsflug von Verkehrsflugzeugen zur Treibstoffeinsparung," [Online]. Available: https://www.dglr.de/publikationen/2016/370376.pdf (visited on 07/01/2022).

[78] S. R. Bieniawski, S. Rosenzweig, and W. B. Blake, "Summary of flight testing and results for the formation flight for aerodynamic benefit program," in *52nd Aerospace Sciences Meeting*, ser. AIAA SciTech Forum, Reston, Virginia: American Institute of Aeronautics and Astronautics, 2014, ISBN: 978-1-62410-256-1. DOI: 10.2514/6.2014-1457.

[79] T. C. Flanzer and S. R. Bieniawski, "Operational analysis for the formation flight for aerodynamic benefit program," in *52nd Aerospace Sciences Meeting*, Reston, Virginia: American Institute of Aeronautics and Astronautics, 2014. DOI: 10.2514/6.2014-1460.

[80] L. M. Nicolai and G. E. Carichner, *Aircraft design*, Englisch, ser. Fundamentals of aircraft and airship design ; volume 1. Reston, Va: AIAA, American Inst. of Aeronautics and Astronautics, 2010, vol. volume 1, xxii, 883 Seiten, Institut für Flugzeugbau, ISBN: 9781600867514.

[81] J Thorbeck, "Manuskript zur integrierten Lehrveranstaltung Flugzeugentwurf I und II," *TU Berlin, Oktober*, 2003.

[82] National Centers for Environmental Information (NCEI), *Wildfires Report | National Centers for Environmental Information (NCEI)*. [Online]. Available: https://www.ncei.noaa.gov/access/monitoring/monthly-report/fire/202112 (visited on 07/11/2022).

[83] United States Environmental Protection Agency (EPA), *Climate Change Indicators: Wildfires*. [Online]. Available: https://www.epa.gov/climate-indicators/climate-change-indicators-wildfires (visited on 07/11/2022).

[84] W. J. Bräunling, *Flugzeugtriebwerke: Grundlagen, Aero-Thermodynamik, ideale und reale Kreisprozesse, Thermische Turbomaschinen, Komponenten, Emissionen und Systeme*. Springer-Verlag, 2015, ISBN: 978-3-642-34538-8. DOI: 10.1007/978-3-642-34539-5.

A Appendix

A.1 Maps of the Fire Scenarios

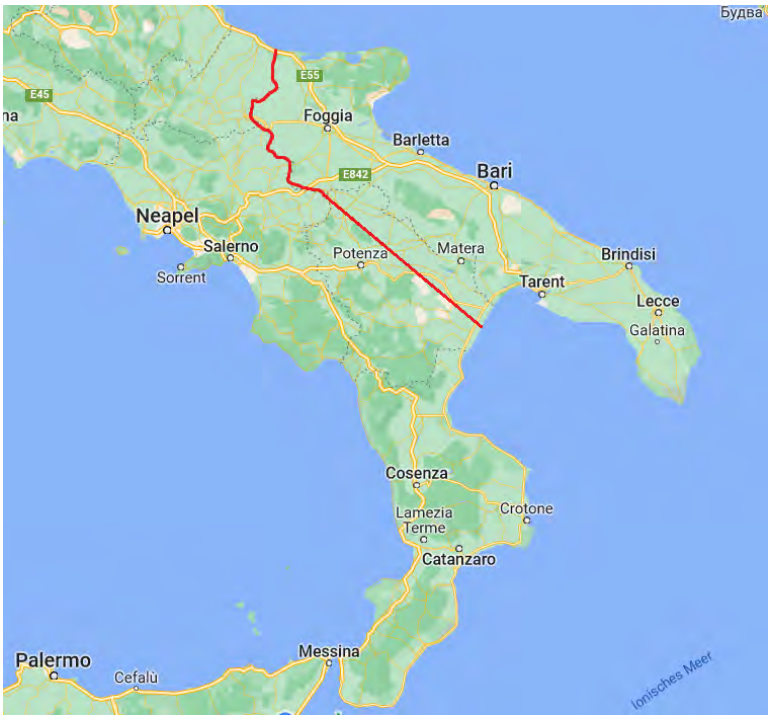

Figure A.1: Map of the coast scenario

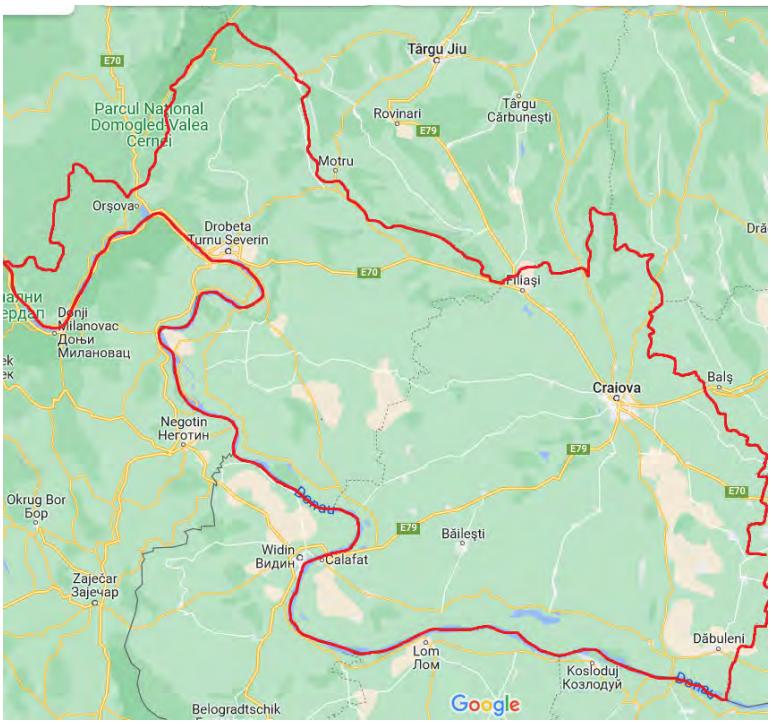

Figure A.2: Map of the domestic scenario

A.2 Neutral Point Calculation

The eq. 13 of Voit-Nitschmann [22] was used for the calculation. The neglect of the fuselage allows $C_{M\alpha f}$ to be set 0 and subsequently the formula simplifies significantly.

$$\frac{\Delta x_N}{l_\mu} = \frac{\frac{-C_{M\alpha_{\mathrm{f}}}}{C_{L_{\alpha\,\mathrm{w}}}} + \left[\xi_{\mathrm{HT}} \cdot \frac{S_{\mathrm{HT}}}{S_{\mathrm{W}}} \cdot \frac{r_{\mathrm{H}}}{l_\mu} \cdot \frac{C_{L_{\alpha\,\mathrm{ht}}}}{C_{L_{\alpha\,\mathrm{w}}}} \cdot \left(1 - \frac{d\alpha_W}{d\alpha}\right)\right] \cdot \frac{r_0}{l_\mu}}{\left[1 + \xi_{\mathrm{HT}} \cdot \frac{S_{\mathrm{HT}}}{S_{\mathrm{W}}} \cdot \frac{r_{\mathrm{H}}}{l_\mu} \cdot \frac{C_{L_{\alpha\,\mathrm{ht}}}}{C_{L_{\alpha\,\mathrm{w}}}} \cdot \left(1 - \frac{d\alpha_W}{d\alpha}\right)\right]} \tag{13}$$

The tailplane efficiency ξ_H is usually between 0.90 and 0.98 [22]. In the design, a conservative value of 0.90 was used. The wing area and the tail area from chap. 4.11. The determination of the lift gradients for wing and tail can be approximated by equation eq. 14.

$$C_{L_\alpha} = \frac{dc_L}{d\alpha} = \frac{2\pi A}{A+2} \tag{14}$$

The downwash estimation was done according to Raymer [29]. The displacement of the neutral point through the fuselage is determined with the help of a diagram [22]. The neutral point of the wing system is transferred to the neutral point of the total system via eq. 15.

$$\frac{\Delta x_{N_{\mathrm{total}}}}{l_\mu} = \frac{\Delta x_N}{l_\mu} + \Delta v_{\mathrm{R}} \tag{15}$$

A.3 Visualization of the Module Montage

Initial state

Step 1

Step 2

Step 3

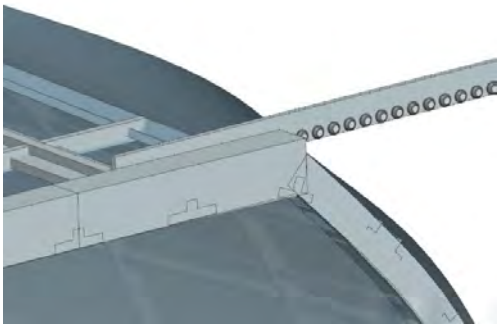

Guide rollers

Step 4

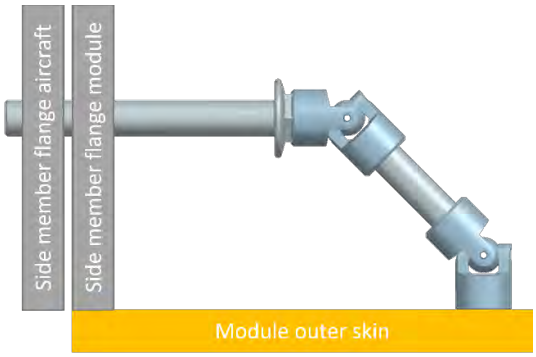

Screwing mechanism

Final state

Figure A.3: Detail steps of the montage

A.4 Battery Sizing: Support Data

The battery advancement trend discussed in the concluding part of the chap. 4.2.5 is elaborated here for further insight into the reference. Fig. A.4 represents the trend adapted from a NASA's report on prospective battery advancements in the area of electric vehicles. The trend is assumed with an 8% yearly increase in the specific energy at cell-level. The loss endured while going from cell-level to pack-level is also vividly represented at two different levels. For INFERNO battery pack calculations, a more realistic 32% loss from cell-level to battery-level was applied [49].

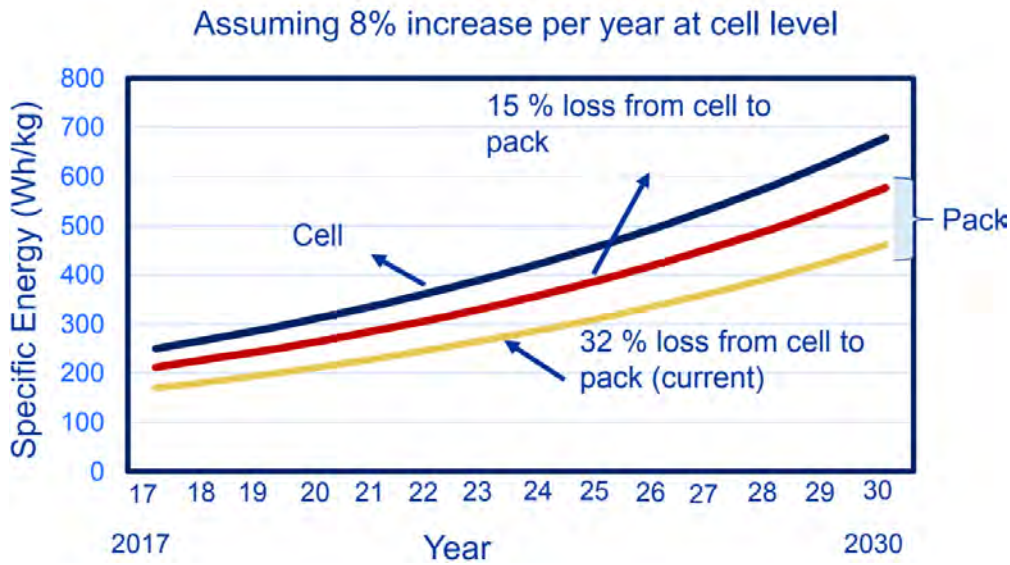

Figure A.4: Trend depicting estimated battery specific energy [W h kg^{-1}] by 2030 at cell-level and pack-level [49]

A.5 INFERNO Cockpit: FOV and Dimensions

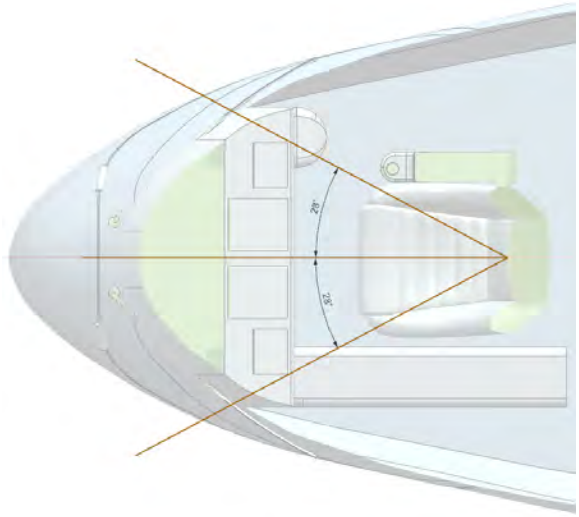

Figure A.5: INFERNO Pilot horizontal FOV

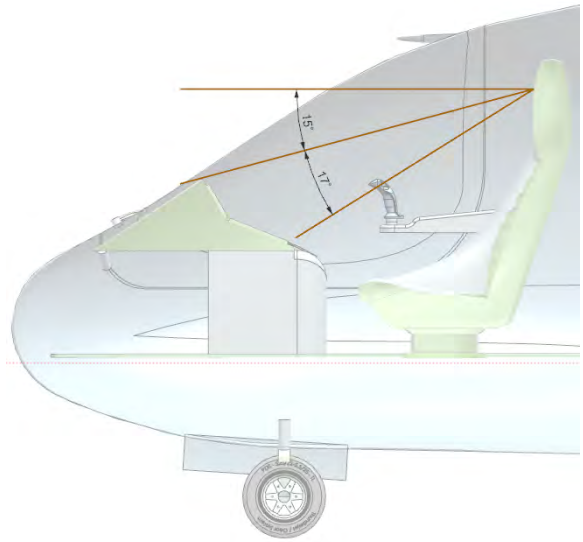

Figure A.6: INFERNO Pilot vertical FOV

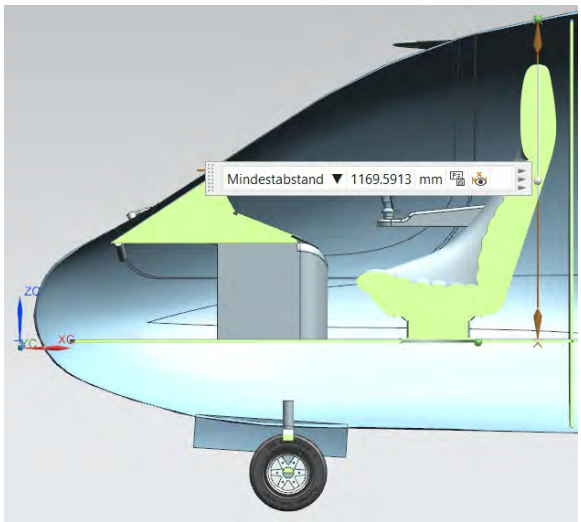

Figure A.7: INFERNO Cockpit: Height in mm

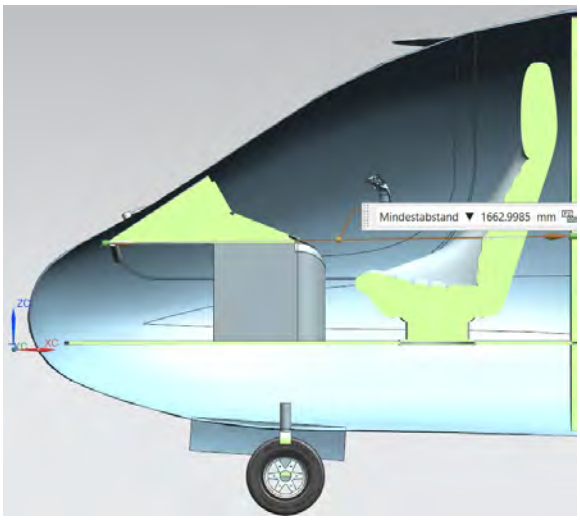

Figure A.8: INFERNO Cockpit: Length in mm

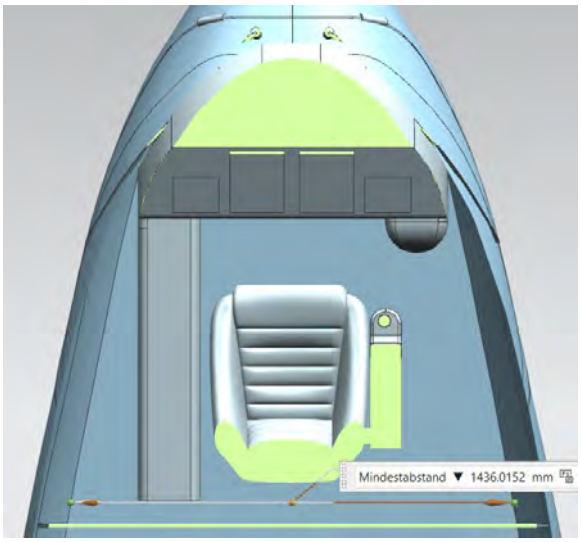

Figure A.9: INFERNO Cockpit: Width in mm

A.6 Data for Fleet Concept

EU	**Copernicus Data (2006 - 2021) [74]**		
Month	Avg. Burned Area [ha/-month]	Avg. Burned Area [m^2/month]	Avg. No. of Fires [1/month]
January	6415	64151428	33
February	15694	156944127	82
March	17131	171313444	102
April	19180	191805000	100
May	4207	42074000	18
June	12978	129788000	41
July	76945	769459000	185
August	106990	1069903000	243
September	41493	414932000	137
October	46061	460617000	65
November	1970	19708000	15
December	1500	15003000	12

Table A.1: Copernicus data for burned area in EU countries (2006 - 2021)

NON-EU	**Copernicus Data (2006 - 2021) [74]**		
Month	Avg. Burned Area [ha/-month]	Avg. Burned Area [$m^2/month$]	Avg. No. of Fires [1/month]
January	3585	35855000	23
February	3496	34957857	14
March	12186	121859365	65
April	40567	405670778	99
May	2728	27285000	13
June	3391	33913000	15
July	37712	377124000	81
August	60425	604249000	132
September	23739	237391000	98
October	13253	132530000	53
November	3231	32306000	23
December	3803	38027000	11

Table A.2: Copernicus data for burned area in Non-EU countries (2006 - 2021)

USA	**National Centers for Environmental Information Data (2001 - 2020) [82], [83]**		
Month	Avg. Burned Area [acres/-month]	Avg. Burned Area [m^2/month]	Avg. No. of Fires [1/month]
January	42954	173828824	1680
February	73366	296901931	3472
March	288955	1169360431	6963
April	373930	1513242360	7273
May	340375	1377449973	7278
June	944599	3822659909	6866
July	1641960	6644782246	8533
August	1780026	7203516018	8124
September	779113	3152961235	5563
October	274960	1112724626	3624
November	243227	984305617	3829
December	217050	878370963	5503

Table A.3: NCEI data for burned area in USA (2001 - 2020)

EU	One INFERNO has the capability of extinguishing 350000 m^2/day. one INFERNO has 4 A/C									
Month	70% of Monthly Burned Area [m^2/month]	Avg. Area Burned per Fire per Month [m^2/fire/month]	Area to be covered per Month [m^2/month]	Area to be covered per Day [m^2/day]	No. of INFERNO FH per day [h/day]	No. of INFERNO Flights [1/Day]	INFERNO Op. Time. [h/day]	Op. INFERNOs. [1/Day]	Redundancy Margin + Humanitarian Aid [+1 INFERNOs]	No. of A/C (on-duty) [1/Day]
January	44906000	1372672	2758260	98509	7	2	9	1	2	8
February	109860889	1336920	6838969	244249	17	4	18	1	2	8
March	119919411	1180180	7953114	284040	19	4	18	1	2	8
April	134263500	1337286	8356900	238769	16	4	18	1	2	8
May	29451800	1609388	1668786	59599	4	1	5	1	2	8
June	90851600	2237724	4356507	155590	11	2	9	1	2	8
July	538621300	2917775	22585742	645307	44	10	23	2	3	12
August	748932100	3084564	30535150	1052936	72	16	18	4	5	20
September	290452400	2123190	14302927	510819	35	8	18	2	3	12
October	322431900	4968134	10336532	295329	20	4	18	1	2	8
November	13795600	913616	1042153	37220	3	1	5	1	2	8
December	10502100	853829	821174	23462	2	1	5	1	2	8

Table A.4: INFERNO Operation estimation based on Copernicus data for EU countries

NON EU	One INFERNO has the capability of extinguishing 350000 m^2/day. One INFERNO has 4 A/C									
Month	70% of Monthly Burned Area [m^2/month]	Avg. Area Burned per Fire per Month [m^2/fire/month]	Area to be covered per Month [m^2/month]	Area to be covered per Day [m^2/day]	No. of INFERNO FH per day [h/day]	No. of INFERNO Flights [1/Day]	INFERNO Op. Time. [h/day]	Op. INFERNOs. [1/Day]	Redundancy Margin + Humanitarian Aid [+1 INFERNOs]	No. of A/C (on-duty) [1/Day]
January	25098500	1103231	1722564	61520	4	1	5	1	2	8
February	24470500	1788966	1314173	46935	3	1	5	1	2	8
March	85301555	13097723	5365705	191632	13	3	14	1	2	8
April	283969544	2858434	12031797	343766	24	5	23	1	2	8
May	19099500	1480581	1128963	40320	3	1	5	1	2	8
June	23739100	1614905	1342764	47956	3	1	5	1	2	8
July	263986800	3259096	10468159	299090	20	4	18	1	2	8
August	422974300	3214090	16890834	582442	40	9	23	2	3	12
September	166173700	1688757	9188731	328169	22	5	23	1	2	8
October	92771000	1753705	5032706	143792	10	2	9	1	2	8
November	22614200	983226	1645668	58774	4	1	5	1	2	8
December	26618900	2464713	1215559	34730	2	1	5	1	2	8

Table A.5: INFERNO Operation estimation based on Copernicus data for Non-EU countries

USA	One INFERNO has the capability of extinguishing 350000 m^2/day. One INFERNO has 4 A/C									
Month	70% of Monthly Burned Area [m^2/month]	Avg. Area Burned per Fire per Month [m^2/fire/month]	Area to be covered per Month [m^2/month]	Area to be covered per Day [m^2/day]	No. of INFERNO FH per day [h/day]	No. of INFERNO Flights [1/Day]	INFERNO Op. Time. [h/day]	Op. INFERNOs. [1/Day]	Redundancy Margin + Humanitarian Aid [+2 INFERNOs]	No. of A/C (on-duty) [1/Day]
January	121680177	72429	34163002	1102032	75	17	18,0	4	6	24
February	207831352	59859	64582026	2306501	158	35	23	7	9	36
March	818552302	117557	177993129	5741714	393	87	23	18	20	80
April	1059269652	145644	205905592	6863520	470	104	23	22	24	96
May	964214981	132483	196940332	6352914	435	97	23	20	22	88
June	2675861936	389726	312489365	10416312	713	158	23	33	35	140
July	4651347572	545101	457336811	14752800	1010	224	23	46	48	192
August	5042461213	620687	463939819	14965801	1025	228	23	47	49	196
September	2207072865	396741	255392347	8513078	583	130	23	27	29	116
October	778907238	214930	123658449	3988982	273	61	23	13	15	60
November	689013932	179946	119957229	3998574	274	61	23	13	15	60
December	614859674	111732	137315209	4429523	303	67	23	14	16	64

Table A.6: INFERNO Operation estimation based on NCEI data for USA

EUROPE Operation [h] and Downtime [h] Calculation for Annual Operation Concept								
Month	Total FFH [h/month]	Total PaxH [h/month]	Total CH [h/month]	Total FH per A/C [h/month]	INFERNO Op. Time [h/year]	Total Downtime [h/month]	Total Downtime [h/year]	Total Hours [h/year]
January	6048,0	4760,0	4032,0	463,8	**6552,6**	208,3	**2207,4**	**8760,0**
February	10080,0	4760,0	4032,0	589,8		82,3		
March	8064,0	4760,0	4032,0	526,8		145,3		
April	15750,0	4760,0	1344,0	682,9		157,1		
May	4032,0	4760,0	4032,0	400,8		271,3		
June	8064,0	4760,0	4032,0	526,8		145,3		
July	15750,0	4760,0	1344,0	682,9		157,1		
August	20880,0	0,0	0,0	652,5		43,5		
September	15120,0	2856,0	1344,0	603,8		68,3		
October	10080,0	4760,0	4032,0	589,8		250,3		
November	4032,0	4760,0	4032,0	400,8		271,3		
December	5040,0	4760,0	4032,0	432,3		407,8		

Table A.7: INFERNO Fleet annual operation hours estimation

USA Firefighting Operation and Downtime Annual Operation Concept				
Total No. of FH [h/month]	Total No. of FH [h/year]	Total No. of FH [h/month]	Total Downtime [h/year]	Total Hours [h/year]
558,0	**8073,0**	186,0	**687,0**	**8760,0**
630,0		42,0		
697,5		46,5		
675,0		45,0		
697,5		46,5		
675,0		45,0		
697,5		46,5		
697,5		46,5		
675,0		45,0		
697,5		46,5		
675,0		45,0		
697,5		46,5		

Table A.8: INFERNO Firefighting Fleet annual operation hours estimation

A.7 Tables Representing LCC & DOC

Parameter	Unit	Value
Sea level static thrust	lbs	4410
Max. Turbine inlet temperature	rankine	3200 [84]
Max. Mach number	-	0.25
Operating Weight Empty (OWE)	lbs	5183
Max. Cruise speed	kts	162
Number of aircraft	-	700
Number of flight tests	-	2
Glass cockpit per aircraft	€	200000
Engineer hours	h	1027788
Prototype construction	€	13644096*
Flight test	€	5730648
Tooling	h	890688
Production	h	6405144
Quality Assurance (QA)	h	832669
Bill of Material (BOM)	€	242055751*
Powertrain	€	3282571*
Life Cycle Cost (LCC)	€	769006025*
EBIT Margin	%	15
LCC per aircraft	€	1463367*

Table A.9: Total LCC and the necessary build-up costs; * represent the costs converted to 1998-€ and then adjusted to assumed inflation of year 2030

Parameter	Unit	Value
Block Time Supplement (BTS)	h	0.083
Fuel price	€/kg	1*
Max. Take-Off Mass (MTOW)	kg	5660
Operational Weight Empty (OWE)	kg	2351
Range	km	1200
Landing fee rate	€/kg	0.01
Ground handling fee rate	€/kg	0.033
Unit rate for navigation	€/km	100
Labor rate	€/h	50
Cost burden	-	2
Insurance rate	-	0.005
Interest rate	-	0.05
Depriciation rate	years	14
Flight time	h	4.5
Flight cycles	1/yr	1059
DOC_{fuel}	€/100km	41.67*
DOC_{fees}	€/100km	64.25*
$DOC_{maintenance}$	€/100km	85.11*
DOC_{crew}	€/100km	65.67*
$DOC_{capital}$	€/100km	34.09*
DOC	€/100km	291.79

Table A.10: Calculated DOC and its important parameters [34]; * represent the costs adjusted to assumed inflation rate of year 2030

A.8 Formulas for Power Demand Calculation

In chap. 4.2.1, the power demand is calculated within the different flight phases with the following formulas, that are taken from "Flugzeugentwurf I" by Prof. Strohmayer [32], "General Aviation Aircraft Design: Applied Methods and Procedures" by Gudmudsson [35] and "Grundlagen der Hubschrauber Aerodynamik" by van der Wall [36]. If not noted otherwise the time for a flight phase was approximated with $t = s/V$ and the fuel consumption with $m_{\text{fuel}} = SFC \cdot P \cdot t$. All calculations consider the electric efficiency and propeller efficiency as described in chap. 4.2.1.

A.8.1 Horizontal Take-off Run:

Calculation of Lift-off speed:

$$V_{\text{LOF}} = 1.1 \cdot \sqrt{\frac{2 \cdot W}{\rho \cdot S_{\text{W}} \cdot C_{\text{Lmax}}}} \tag{16}$$

Calculation of acceleration during take-off run:

$$\frac{\mathrm{d}V}{\mathrm{d}t} = \frac{{V_{\text{LOF}}}^2}{2 \cdot l_{\text{to}}} \tag{17}$$

Lift at average airspeed:

$$L = \frac{\rho}{2} \cdot v^2 \cdot S_{\text{W}} \cdot C_{\text{L}} \tag{18}$$

Drag at average airspeed:

$$D = \frac{\rho}{2} \cdot v^2 \cdot S_{\text{W}} \cdot C_{\text{D}} \tag{19}$$

Thrust during take-off run:

$$T_{\text{TO}} = \frac{\mathrm{d}V}{\mathrm{d}t} \cdot \frac{W}{g} + D + \mu \cdot (W - L) \tag{20}$$

Calculation of power during take-off run:

$$P_{\text{TO}} = T_{\text{TO}} \cdot \frac{V_{\text{LOF}}}{\sqrt{2}} \tag{21}$$

A.8.2 Horizontal Climb:

Calculation of power during climb in horizontal flight:

$$P_{\text{Cl}} = (\sin\gamma + \epsilon) \cdot v_{\text{climb}} \cdot m \cdot g \tag{22}$$

A.8.3 Cruise:

Calculation of power during cruise flight:

$$P_{\text{Cruise}} = (\epsilon \cdot \frac{m \cdot g}{v_{\text{cruise}}}) \tag{23}$$

Calculation of fuel consumption during cruise flight (brequet equation):

$$m_{\text{fuel}} = m - \frac{m}{\exp l \cdot SFC \cdot \epsilon / \eta_{\text{prop,EM}}} \tag{24}$$

A.8.4 Horizontal Descend :

Calculation of power during descend in horizontal flight:

$$m_{\text{fuel}} = m - \frac{m}{\exp l \cdot SFC \cdot \epsilon / \eta_{\text{prop,EM}}} \tag{25}$$

A.8.5 Hovering:

Calculation of required power for hovering:

$$P_{\text{hov}} = m \cdot g \cdot \sqrt{\frac{m \cdot g}{2 \cdot \rho \cdot A_{\text{prop}}}}) \tag{26}$$

A.8.6 Vertical Ascend and Descend:

Calculation of required power for vertical flight

$$P_{\text{VTOL}} = \frac{P_{\text{hov}}}{\frac{v_{\text{i}}}{v_{\text{i0}}}} \tag{27}$$

$$\frac{v_{\text{i}}}{v_{\text{i0}} = -\frac{v_{\text{vert}}}{2 \cdot v_{\text{i0}}} + \sqrt{(\frac{v_{\text{vert}}}{2 \cdot v_{\text{i0}}})^2 + 1}} \tag{28}$$

$$v_{\text{i}} = \sqrt{\frac{m \cdot g}{2 \cdot \rho \cdot A_{\text{prop}}}} \tag{29}$$

For vertical descending the same formula is used with a negative vertical speed.

A.9 Formulas for Weight Calculation

Wing Weight:

$$W_{\mathrm{W}} = 96.948 \cdot \left[\left(\frac{n_{\mathrm{z}} W_0}{10^5} \right)^{0.65} \left(\frac{A}{\cos^2 \Lambda} \right)^{0.57} \times \left(\frac{S_{\mathrm{W}}}{100} \right)^{0.61} \left(\frac{1+\lambda}{2\frac{t}{c}} \right)^{0.36} \sqrt{1 + \frac{v_{\mathrm{H}}}{500}} \right]^{0.993} \tag{30}$$

Horizontal Tail Weight:

$$W_{\mathrm{HT}} = 127 \left[\left(\frac{n_{\mathrm{z}} W_0}{10^5} \right)^{0.87} \left(\frac{S_{\mathrm{HT}}}{100} \right)^{1.2} \left(\frac{l_{\mathrm{HT}}}{10} \right)^{0.483} \sqrt{\frac{b_{\mathrm{HT}}}{t_{\mathrm{HT\,max}}}} \right]^{0.458} \tag{31}$$

Vertical Tail Weight:

$$W_{\mathrm{VT}} = 98.5 \left[\left(\frac{n_{\mathrm{z}} W_0}{10^5} \right)^{0.87} \left(\frac{S_{VT}}{100} \right)^{1.2} \sqrt{\frac{b_{\mathrm{VT}}}{t_{\mathrm{VT\,max}}}} \right] \tag{32}$$

Fuselage Weight:

$$W_{\mathrm{FUS}} = 200 \left[\left(\frac{n_{\mathrm{z}} W_0}{10^5} \right)^{0.286} \left(\frac{l_{\mathrm{F}}}{10} \right)^{0.857} \left(\frac{w_{\mathrm{F}} + d_{\mathrm{F}}}{10} \right) \left(\frac{v_{\mathrm{H}}}{100} \right)^{0.338} \right]^{1.1} \tag{33}$$

Landing Gear Weight:

$$W_{\mathrm{MNLG}} = 0.054 \left(n_{\mathrm{l}} W_{\mathrm{l}} \right)^{0.684} \left(L_{\mathrm{m}}/12 \right)^{0.601} \tag{34}$$

Installed Engine Weight:

$$W_{\mathrm{EI}} = 2.575 {W_{\mathrm{ENG}}}^{0.922} N_{\mathrm{ENG}} \tag{35}$$

Fuel System Weight:

$$W_{\mathrm{FS}} = 2.49 \left[{Q_{\mathrm{tot}}}^{0.6} \left(\frac{Q_{\mathrm{tot}}}{Q_{\mathrm{tot}} + Q_{\mathrm{int}}} \right)^{0.3} {N_{\mathrm{TANK}}}^{0.2} {N_{\mathrm{ENG}}}^{0.13} \right]^{1.21} \tag{36}$$

Flight Control-system Weight:

$$W_{\mathrm{CTRL}} = 1.08 {W_0}^{0.7} \quad \text{(Powered control system)} \tag{37}$$

$$W_{\mathrm{CTRL}} = 1.066 {W_0}^{0.626} \quad \text{(Manual control system)} \tag{38}$$

Avionics Systems Weight:

$$W_{\mathrm{AV}} = 2.117 {W_{\mathrm{UAV}}}^{0.933} \tag{39}$$

Electrical System:

$$W_{\mathrm{EL}} = 12.57 \left(W_{\mathrm{FS}} + W_{\mathrm{AV}} \right)^{0.51} \tag{40}$$

Air-conditioning and Anti-icing:

$$W_{\mathrm{AC}} = 0.265 {W_0}^{0.52} {N_{\mathrm{OCC}}}^{0.68} {W_{\mathrm{AV}}}^{0.17} Ma^{0.08} \tag{41}$$

Furnishings:

$$W_{\mathrm{FURN}} = 34.5 N_{\mathrm{c}} {q_{\mathrm{H}}}^{0.25} \tag{42}$$

A.10 Static Margin and Position of the Center of Gravity

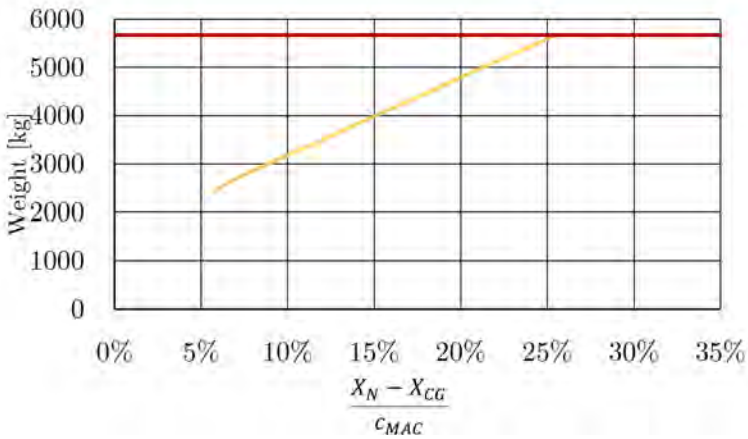

Figure A.10: Static margin for maximum payload

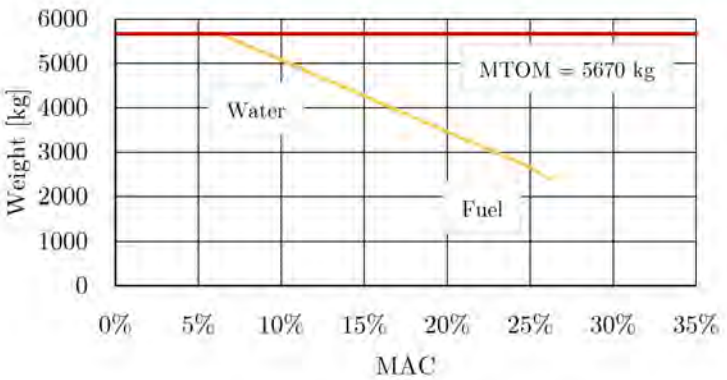

Figure A.11: Shift of the CoG for maximum payload

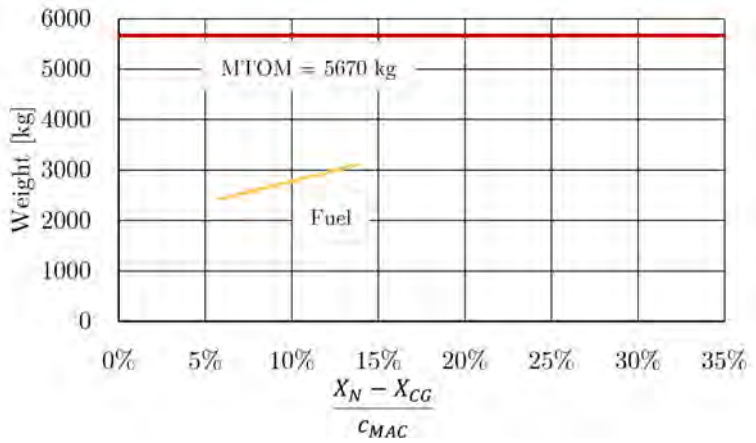

Figure A.12: Static margin for ferry range

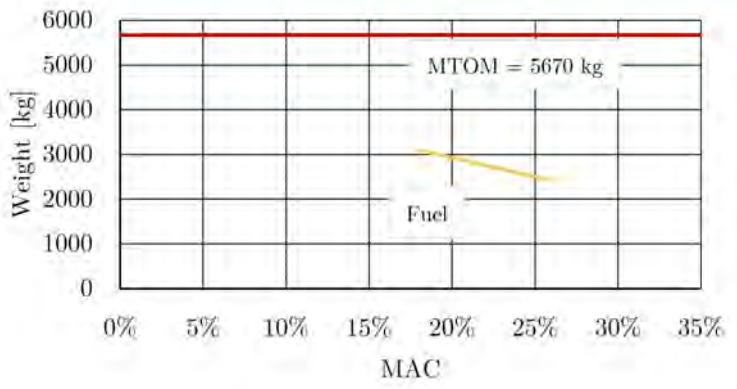

Figure A.13: Shift of the CoG for ferry range

A.11 Landing Gear

The INFERNO aircraft features a conventional landing gear configuration with a nose landing gear and two main landing gears. When positioning and sizing the landing gear, specific load assumptions have to be considered. Typical nose landing gear loads should be in the range of 5 % of MTOW at the aftmost CoG position and 20 % of the MTOW in order to easily lift of the aircraft's nose during takeoff while guaranteeing enough nose wheel traction for taxiing and steering. Typical values for the nose wheel loads are 8 % of MTOW at the aftmost CoG position and 15 % of the MTOW at the most forward CoG position. The maximum and minimum static loads can be calculated with eq. 43 to 45. The gear loads for different mission types for the initial aircraft design and the re-design after the trade studies can be found in tab. A.11. For the MTOM scenario with the water tanks filled completely, the nose gear loads are relatively high but still within the margin suggested in the literature.

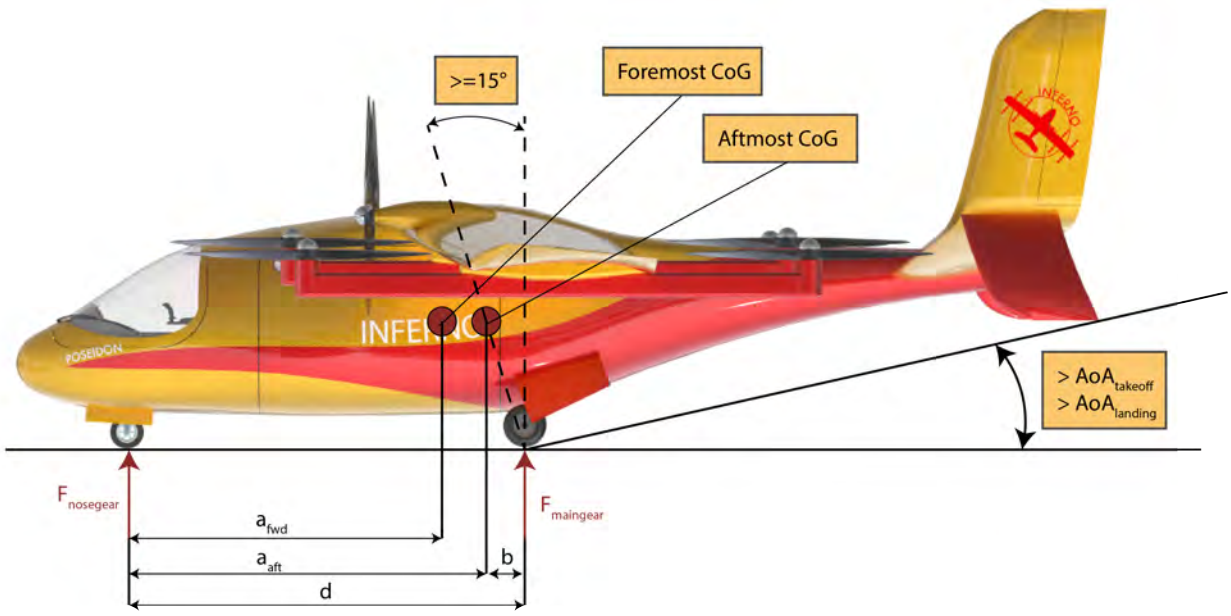

Figure A.14: Landing gear requirements

$$F_{\text{maingear}} = m_{\text{MTOW}} \cdot \frac{d-b}{2d} \tag{43}$$

$$F_{\text{nosegear}_{\text{max}}} = m_{\text{MTOW}} \cdot \frac{d-a_{fwd}}{d} \tag{44}$$

$$F_{\text{nosegear}_{\text{min}}} = m_{\text{MTOW}} \cdot \frac{d-a_{aft}}{d} \tag{45}$$

		$\mathbf{CoG_{FWD}}$		$\mathbf{CoG_{AFT}}$	
		Total weight [kg]	Percentage [%]	Total weight [kg]	Percentage [%]
MPL	Nose gear	1100.18	19.4	756	13.33
	Main gear	4569.82	80.6	4914	86.67
FERRY	Nose gear	979.36	17.2	756	13.33
	Main gear	4690.64	82.8	4914	86.67

Table A.11: Total gear loads for most-aft and most-forward CoG for initial design

Furthermore, additional requirements have to be met when considering the landing gear and its positioning. To guarantee the stability on ground, the position of the main landing gear should always be behind the aftmost position of the CoG. According to Raymer [29] , the tipback angle should be at least 15°. This angle is considered as the angle between a vertical line from the main gear and a line between the wheel position and the aftmost CoG position.

As an additional requirement for the landing gear position, the takeoff and landing phase and their **A**ngle **o**f

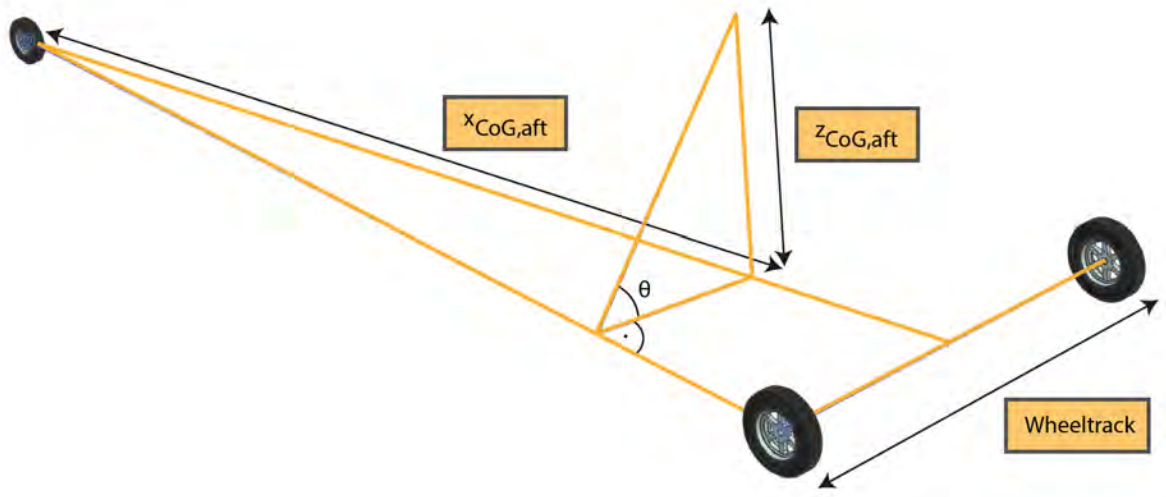

Figure A.15: Calculation of turnover angle

Attacks (AoAs) have to be considered. To achieve the necessary lift coefficient during these phases, a specific AoA has to be flown. In order to prevent a tail strike, the tail down angle has to be larger than the flown AoA. Furthermore, the tipback angle has to be larger than the taildown angle.

Besides considering the taildown and tipback angle, the bank angle clearance has to be investigated. Since the INFERNO is featuring a high wing configuration, this criteria can easily be met and the minimum bank angle of 6° to 8° which is required according to Scholz [31] can be achieved. Moreover, the engine ground clearance of at least 0.5 m has to be obtained which is achieved in the design. Moreover, the turnover angle also known as the tilt angle has to be in a specific range. It is measuring the aircraft's tendency to overturn during taxiing. The tilt angle of the airplane has a value of 54.5°. The tilt angle was calculated using data from the 3 view drawing as well as the calculation of the z-position of the CoG as shown in fig. A.15.

A.12 v-n Diagram

In order to create a v-n diagram, the first step is to determine the load limiting flight speeds. The load for the stall speed v_{stall} must be 1 [29]. At low flight speed the load is limited by the velocity v_A that is caused by the highest AoA without stalling. The flight speed v_A is known as maneuvering speed and can be derived from the stall speed as depicted in eq. 46 [22]. The maximum possible speed is called v_D. It specifies the point of maximum dynamic pressure or, depending on the aircraft type, the point of maximum temperature [29] and is important for the structural design of the aircraft. According to Raymer, the maximum possible speed for subsonic aircraft is typically 50 % higher than the cruise speed. Lastly, the cruise speed is given by the sizing chart in Figure 4.21. Typical values for the load factors were chosen according to Raymer [29].

$$v_A \geq v_{\text{stall}} \sqrt{\text{n}_{\text{lim}_{\text{pos}}}} \tag{46}$$

After the speeds were determined, the gust loads needed to be calculated. When an aircraft experiences a gust, the result is a change in the AoA that increases or decreases the load. Raymer [29] developed a method to derive an estimation of the gust load. Therefore the mass ratio μ is calculated from the known design parameters as shown in eq. 51. With its help the gust alleviation factor K_g is determined in eq. 50. This statistical factor corrects the load, as the gust usually induces a cosine-like intensity increase, giving the pilot time to react and thus decreasing the load effect [29]. Subsequently, the gust velocities are determined with fig. A.16 and the final gust loads for the specific velocities can be found according to eq. 48 and 47. It is important to note, that W represents the weight force and not the MTOW in the following equations.

$$n_{\text{gust}} = 1 \pm \Delta n \tag{47}$$

$$\Delta n = \frac{\rho U v C_{L_a}}{2W/S_{\text{W}}} \tag{48}$$

$$U = K_g U_{de} \tag{49}$$

$$K_g = \frac{0.88\mu}{5.3 + \mu} \tag{50}$$

$$\mu = \frac{2\,(W/S_{\text{W}})}{\rho G C_{L_a}} \tag{51}$$

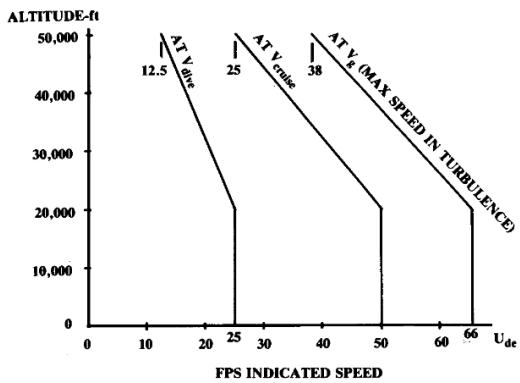

Figure A.16: Typical equivalent gust velocities for transport aircraft [29]

Fig. 4.18 shows the determined v-n diagram for the aircraft design. Point A represents the load during the maneuver speed v_A, the points D and E are defined by the nose dive speed v_D and $\text{n}_{\text{lim}_{\text{pos}}}$. The points B, C, F and H display the gust loads for the cruise velocity and the nose dive velocity. The v-n diagram shows, that the initial aircraft design must withstand maximum gust loads of -0.77 to 2.77 in the airspeeds design range.

A.13 Airfoil Data

In the following all drag polars of the E423M and E545 airfoil, and the coordinates of the E423M will be illustrated.

Drag Polars

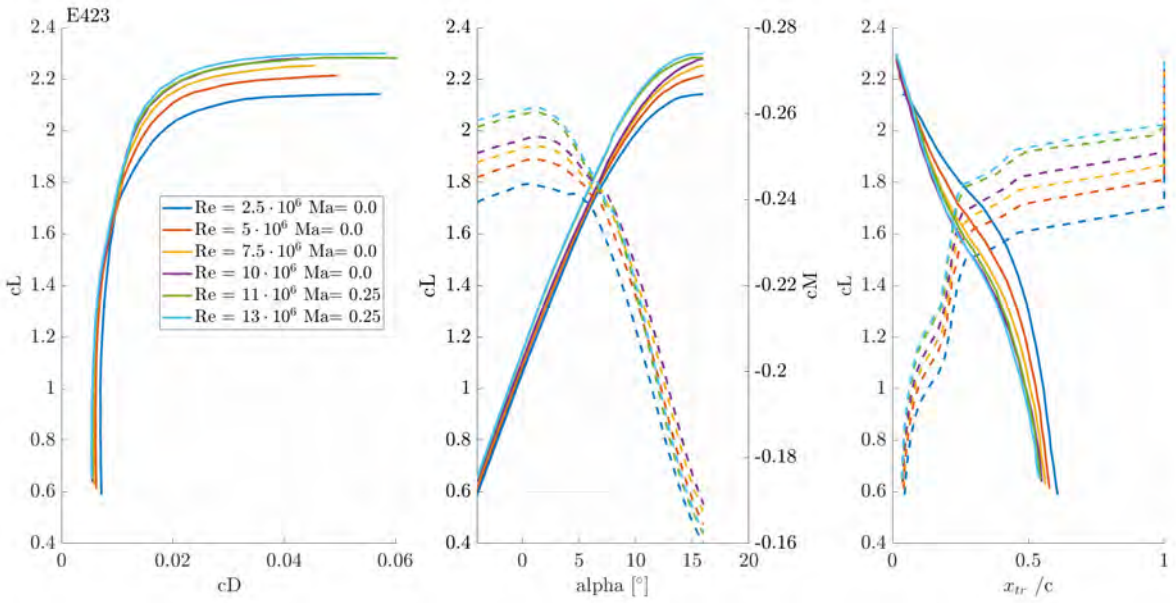

Figure A.17: Drag Polar of the E423M airfoil for Re = 2.5-13 · 10^6 and Ma = 0-0.25

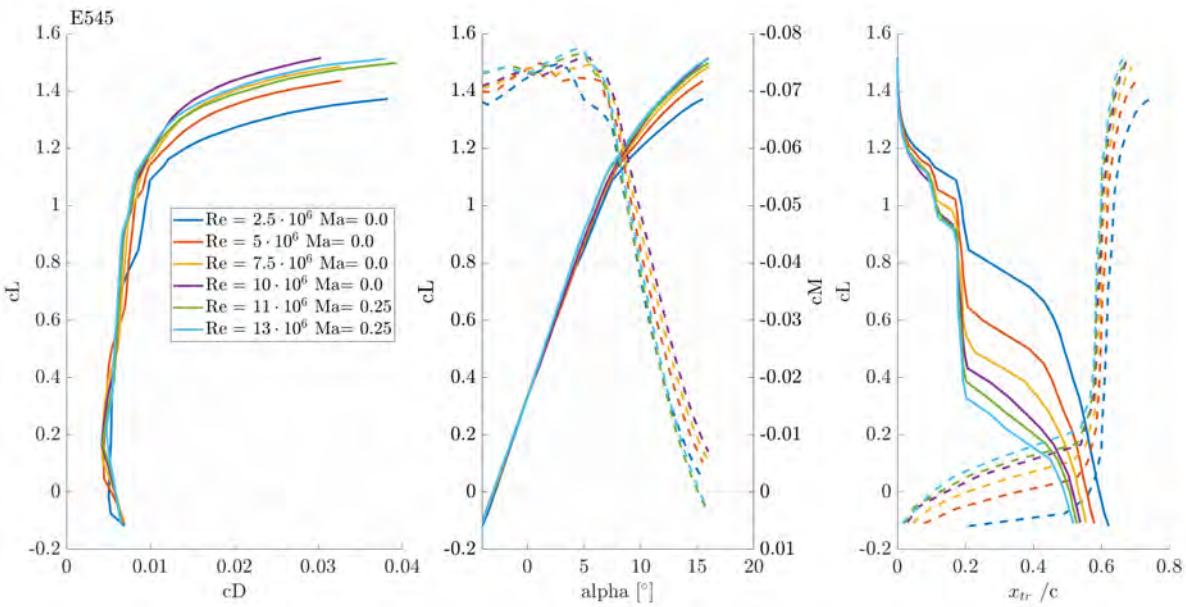

Figure A.18: Drag Polar of the E545 airfoil for Re = 2.5-13 · 10^6 and Ma = 0-0.25

E423M Coordinates

E423M Profile Coordinates	
X-Coordinate	Y-Coordinate
1	0
0.994419	0.003981
0.985426	0.009798
0.975923	0.015563
0.965935	0.021025
0.955375	0.026099
0.944044	0.030843
0.931795	0.035353
0.918508	0.03979
0.904166	0.0442
0.888898	0.048634
0.872806	0.053046
0.856094	0.057436
0.83885	0.061778
0.821256	0.066063
0.803351	0.070284
0.785277	0.074432
0.767025	0.078499
0.748694	0.082491
0.730266	0.086392
0.711814	0.090221
0.693344	0.093941
0.674879	0.097579
0.656463	0.101092
0.638066	0.1045
0.619758	0.107776
0.601504	0.110913
0.583374	0.113913
0.565387	0.116731
0.547556	0.119374
0.529942	0.1218
0.512502	0.123987
0.495235	0.125924
0.478083	0.127584
0.460998	0.128988
0.443991	0.130119
0.427012	0.130978
0.410079	0.131575
0.393182	0.131889
0.376312	0.131937
0.359503	0.131709
0.342732	0.131199
0.32603	0.130417
0.309397	0.129343
0.292837	0.127992
0.276372	0.126347
0.259992	0.124415
0.243737	0.122199

0.22762	0.119697
0.211703	0.116924
0.196026	0.11387
0.180648	0.110552
0.165629	0.106963
0.151029	0.103125
0.136926	0.099041
0.123392	0.094748
0.110524	0.090269
0.098399	0.085655
0.087104	0.080954
0.076691	0.076224
0.067203	0.071525
0.058637	0.066905
0.050969	0.062412
0.044149	0.058066
0.038103	0.053896
0.032764	0.049904
0.028053	0.046087
0.023896	0.042447
0.020232	0.038969
0.017003	0.035642
0.014157	0.032457
0.011655	0.029401
0.009462	0.026461
0.007546	0.02363
0.00588	0.020900
0.004448	0.018261
0.003236	0.015706
0.002226	0.013231
0.001406	0.010834
0.000772	0.008510
0.000328	0.006257
0.000066	0.004076
-0.000011	0.0019740
0.000135	-0.000119
0.000616	-0.002202
0.001523	-0.004200
0.002824	-0.006058
0.004422	-0.007795
0.006252	-0.009447
0.008292	-0.011030
0.010542	-0.012545
0.013011	-0.013981
0.015719	-0.015312
0.01869	-0.016508
0.021947	-0.017550
0.025512	-0.018438
0.029423	-0.019169
0.033726	-0.019749
0.038485	-0.020196
0.043777	-0.020515
0.049701	-0.020685
0.056386	-0.020684
0.063985	-0.020503
0.072665	-0.020105
0.082605	-0.019455

0.093924	-0.018552
0.106624	-0.017346
0.120583	-0.015840
0.135502	-0.014014
0.151149	-0.011841
0.16733	-0.009311
0.18409	-0.006388
0.201414	-0.003208
0.21896	0.000029
0.236471	0.003075
0.254105	0.005894
0.271969	0.008532
0.290228	0.011021
0.308961	0.013485
0.32794	0.015970
0.346931	0.018455
0.365738	0.020928
0.384206	0.023274
0.40242	0.025430
0.42043	0.027398
0.438294	0.029136
0.456201	0.030652
0.474211	0.032000
0.492289	0.033171
0.510542	0.034163
0.52901	0.035038
0.54757	0.035804
0.566252	0.036441
0.585058	0.037001
0.603813	0.037480
0.622544	0.037830
0.641277	0.038092
0.65986	0.038253
0.678355	0.038258
0.696799	0.038148
0.715056	0.037904
0.733222	0.037471
0.751316	0.036899
0.769219	0.036154
0.787061	0.035195
0.8048	0.034085
0.822357	0.032760
0.839838	0.031236
0.857059	0.029552
0.874016	0.027637
0.890599	0.025583
0.906617	0.023320
0.92201	0.020918
0.936517	0.018354
0.950111	0.015661
0.962619	0.012832
0.974103	0.009868
0.984548	0.006674
0.994111	0.003108
1	0

A.14 INFERNO Immersion

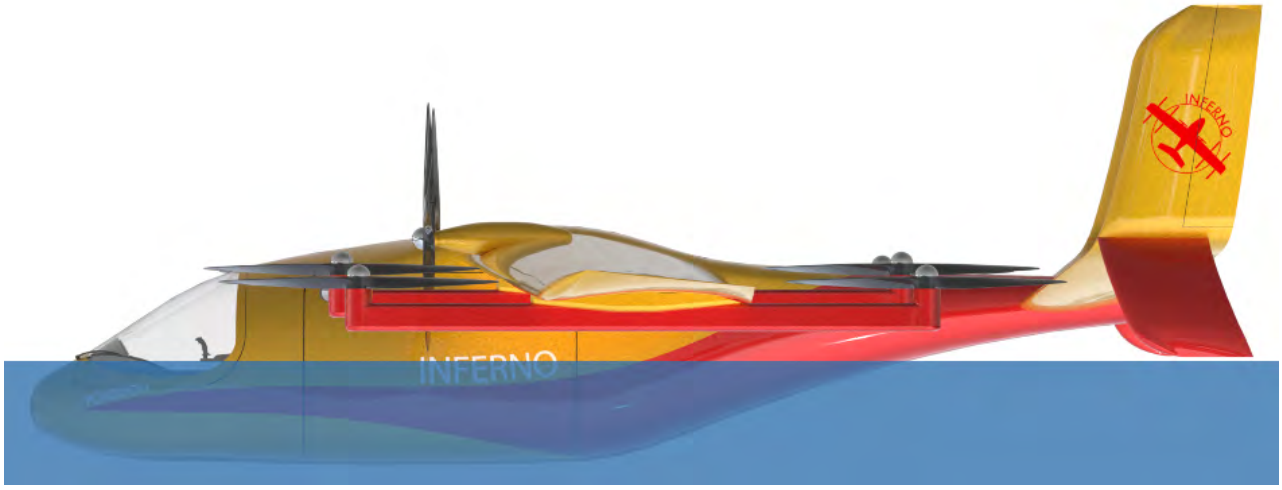

Figure A.19: INFERNO at maximum immersion depth